Micromechanical analyses on bending of polysynthetically twinned single crystal of titanium aluminide

Z. Wang, W.H.Wong, T.F. Guo*

*Institute of High Performance Computing, A*STAR, 138632, Singapore*

Abstract

Micromechanical bending analyses *via* CPFEM of polysynthetically twinned (PST) single crystal of TiAl composing of one α_2–phase lamella and six γ–phase lamellae have been performed. The results have demonstrated that a decrease in the domain size aspect ratio λ_D/λ_L or an increase in the volume fraction of α_2 phase f_{α_2} have an effect of increasing the induced bending moment and consequently bending resistance under both bending modes of hogging and sagging. The similar variations in λ_D/λ_L and f_{α_2} results in a decreasing trends of maximum tensile and compressive initial yield stresses (normal bending stresses), obtained through small strain beam theory. Results have also shown the effects of imposed constraints on the bending behavior; traction–free boundary conditions results in activation of prismatic slips instead of pyramidal slips in α_2–phase, leading to a lower observed bending moment for the variables λ_D/λ_L and f_{α_2} considered. A scaling law is proposed that relates bending moment to domain size aspect ratio and bending angle.

Keywords: Lamellar TiAl; Crystal plasticity; Micromechanical bending analyses; Domain size aspect ratio; Volume fraction

---

1. Introduction

Titanium aluminide alloys comprising γ-TiAl and the α_2-Ti$_3$Al phases exhibit promising potential in high-temperature and lightweight applications such as in automotive, aero-engines, gas turbines (Cao et al., 2010; Gu and Greer, 2015; Chen et al., 2016; Schütze, 2016; Zeng and Li, 2021). The two–phase TiAl alloys contain a minor volume fraction of the α_2-Ti$_3$Al phase (e.g., Fujiwara et al., 1990; Inui et al., 1992a; Kabir et al., 2010; Appel et al., 2011), generally less than 20% (Grujicic and Batchu, 2001; Zhu et al., 2006; Mine et al., 2011; Cornec et al., 2015) and up to 32% (Dimiduk et al., 1998). The major constituent γ-TiAl typically accounts for 80 to 90% of the total volume fraction in TiAl alloys (Werwer et al., 2007) for a balanced property. Two–phase TiAl alloys can be manufactured with different microstructures, including near γ, duplex, nearly lamellar and fully lamellar (Kim, 1992). Of all the possible microstructures, lamellar TiAl alloys are considered the most promising candidate for many applications as they offer attractive physical and mechanical properties, such as low density, excellent high temperature creep resistance, excellent oxidation and fatigue resistance and high specific strength (Appel and Wagner, 1998; Kim, 1998; Yamaguchi et al., 2000; Schwaighofer et al., 2014; Chlupova et al., 2020).

---

*Corresponding author

Email address: `guotf@ihpc.a-star.edu.sg` (T.F. Guo)

Despite its outstanding properties that are comparable to nickel–based superalloys, lamellar TiAl alloys suffers from poor ductility, largely due to the anisotropy of the constituent microstructure (Arata et al., 2001; Werwer and Cornec, 2006; Chen et al., 2019), thereby limiting their applications. As such, extensive and intense efforts have been dedicated to further our understanding of its microstructure–property relationship, on both experimental (e.g. Liu et al., 2010; Zong et al., 2015; Li et al., 2018; Yu et al., 2020; Song et al., 2020, among many others) and numerical fronts. In the latter, several numerical approaches spanning different length–scales have been utilized such as phase–field model (e.g Wang et al., 2019; Teng et al., 2012), molecular dynamics simulation (e.g Kanani et al., 2016; Li et al., 2019; Zeng and Li, 2021) and finite element method, specifically the Crystal Plasticity Finite Element Method (CPFEM). Guided by experimental inputs and observations, CPFEM has proven to be an effective and versatile tool for describing deformation mechanisms and mechanical responses of crystalline materials, and in this context lamellar TiAl crystals (e.g Kad et al., 1995; Schlögl and Fischer, 1997; Lebensohn et al., 1998; Werwer and Cornec, 2000; Grujicic and Batchu, 2001; Grujicic et al., 2003a,b; Werwer and Cornec, 2006; Zambaldi et al., 2011; Cornec et al., 2015; Su et al., 2016; Ma et al., 2018; Chen et al., 2019, among many others). Mechanical responses of lamellar TiAl crystals have almost always been investigated by subjecting a Representative Volume Element (RVE) or a unit cell to uniaxial tension–compression loads. These deformation modes are standard benchmark tests for material characterization, and have provided much insights to the microstructure–property relationships of TiAl crystals, as evident in the large body of literature available. However, there are other benchmark tests such as bending (3–point and 4–point) and torsion tests that need to be performed in order to better understand the microstructure–property relationships, so as to enhance the commercial and industrial applicabilities of TiAl alloys.

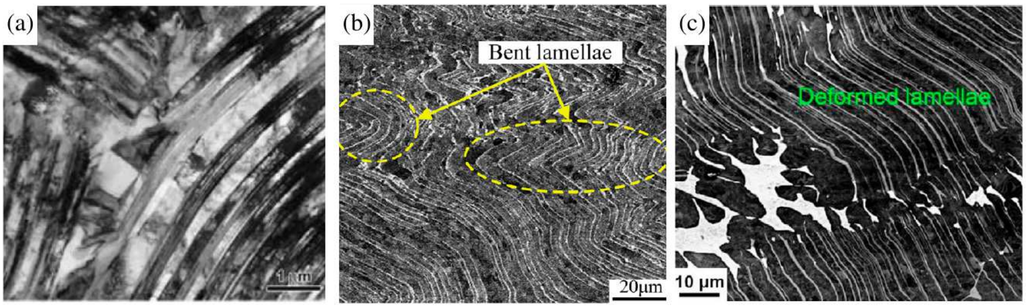

Fig. 1. Bent lamellae observed from (a) TEM micrographs of Ti-47Al-xH alloys compressed with the strain rate of $0.01s^{-1}$ above 1000°C (Liu et al., 2010); (b) SEM micrographs of Ti-46Al-2V-1Cr-0.3Ni compressed to $\varepsilon = 63\%$ with the strain rate of $0.01s^{-1}$ at 1323K (Zong et al., 2015); and (c) SEM micrograph of Ti-45Al-8.5Nb-0.2W-0.2B-0.02Y compressed at 800 °C to $\varepsilon = 30\%$ (Song et al., 2020).

Shear strain and heavy bending in lamellar TiAl alloys can be induced by large deformations during hot working processes (Huang, 2005). Fig. 1 displays the Transmission Electron Microscopy (TEM) and Scanning Electron Microscopy (SEM) micrographs that clearly show the bent lamallae in PST TiAl alloys composing of lamellar α_2 and γ that have been compressed/forged at various strain rates at elevated temperatures ($>$ 1000°C). It is interesting to note from Fig. 1(b) the severe bending/kinking of the lamallae (Zong et al., 2015), as well as the observed buckling of the lamallae in Fig. 1(c), attributable to the deformation anisotropy of the lamellar structure (Song et al., 2020). Zhang et al. (1998) has reported misoriented, non-coherent α_2/γ interfaces in severely bent lamallae in their analyses of hot deformation behavior of lamellar TiAl microstructure, wherein the TiAl has been hot forged to about 60%

reduction at a deformation condition of 1050°C/0.001s^{-1}. The analyses of grain orientations in hot–compressed Ti–46Al–8Nb alloys have indicated high local strain with high dislocation density and distortion energy are associated with bending of lamallae (Li et al., 2018). Bending of lamellae is not only observed under compression but under tension as well. Yu et al. (2020) have reported (see Fig. 8 therein) bent lamellae of Ti-45Al-9Nb at a temperature of $1150°C$ in the strain rate range of 0.0004-$0.0025s^{-1}$. From the abovementioned, it is apparent that bending of lamellae in PST TiAl alloys can be induced by heavy deformation at elevated temperatures, and consequently influencing the mechanical performance of these alloys e.g. slip movements, strain localization etc. This provides the motivation for this work and that is to investigate the macroscopic bending responses or behavior of lamellar PST TiAl crystals *via* micromechanical analyses using crystal plasticity–based constitutive model. Here the following effects on the bending behavior will be investigated:

- effect of length scale i.e. aspect ratio between domain size and lamellar thickness,
- effect of volume fraction of α_2 phase, and
- effect of lateral constraints i.e. bending under conditions of plane strain and plane stress.

While there may be unanswered material science questions regarding lamellar PST TiAl crystals under different deformation modes, this paper focuses on the mechanics and the multi-scale methodology and implementation to model bending of the RVE. To the authors' knowledge, three–dimensional micromechanical CPFEM analyses of bending of lamellar PST TiAl crystals have not been attempted before, though Kouznetsova et al. (2002) has demonstrated a computational homogenization scheme to obtain the local higher–order stress response of a voided RVE subjected to macroscopic bending. It is worthwhile to note that multi–scale homogenization involving large spatial deformation gradients at macroscopic scale e.g. in bending (and torsion), can be classified as second–order homogenization, wherein the macroscopic deformation gradient tensor and its Lagrangian gradient are passed to the RVE, and importantly the microscopic length scale can be accounted for. This is in contrast to the first–order homogenization that is well–established and widely used in boundary value problem where periodic boundary conditions are enforced e.g. uniaxial tension and compression, and shear, such that only the macroscopic deformation gradient needs to be passed to the RVE (Geers et al., 2010). The present cell analysis on bending is formulated in–between the first– and second–order homogenization.

The outline of this paper is as follows. Section 2 describes the modeling aspects of the unit cell including the deformation systems in the PST crystal of TiAl, the crystal plasticity constitutive model adopted and the numerical impletmentation of the boundary and loading conditions to effect the bending of the unit cell. Section 3 presents the results and findings obtained from the micromechanial analyses. The paper concludes with some remarks in Section 4.

2. Modelling aspects

This section presents the formulation of the problem under study. Subsection 2.1 describes the construction of the three–dimensional unit cell representing a single PST TiAl colony. It is composed of one α_2 and 6γ layer(s), where each γ layer is made up of hexagonal–shaped domains. The colony is characterized by two length scales namely lamellar thickness and domain size. The deformation systems of the α_2 and γ phases are detailed in Subsection 2.2, following which in Subsection 2.3 a brief introduction of the crystal plasticity model adopted in this study. Section 2 concludes with the description of the numerical implementation of the micromechanical model, including the boundary and loading conditions to be enforced and applied respectively in Subsection 2.4. The computations are performed using the general–purpose finite element program ABAQUS Version 6.14 within the finite strain setting.

2.1. Three–dimensional unit cell

Consider a cuboid representative volume element (RVE) of initial dimensions $2L_1 \times 2L_2 \times 2L_3$ representing lamellar PST microstructures with the Cartesian coordinate system (X_1, X_2, X_3) with its origin located at the center of the RVE. The proposed RVE, as illustrated in Fig. 2, consists of a bottommost α_2-Ti$_3$Al layer and six γ-TiAl layers stacked on top of the former. The lamellae of two phases are parallel, following Blackburn orientation relationship $\{111\}_\gamma \parallel (0001)_{\alpha_2}$ and $\left\langle 1\bar{1}0 \right]_\gamma \parallel \left\langle 11\bar{2}0 \right\rangle_{\alpha_2}$ (Blackburn, 1970). The global coordinate system shown in the figure depicts the directional convention adopted.

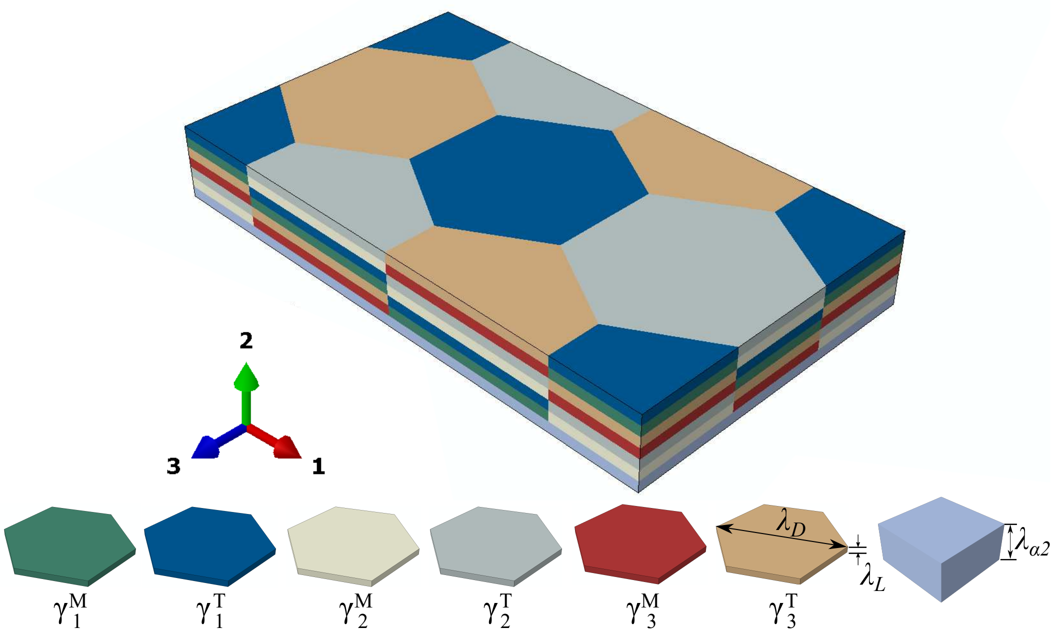

Fig. 2. Representative volume element (RVE) consisting of a α_2-Ti$_3$Al and six γ-TiAl layers. The lamellae of two phases are parallel, obeying the Blackburn orientation relationship. The periodic $\alpha_2 + 6\gamma$-substructures incorporate six variants of γ phase and a unifrom α_2 phase. λ_D and λ_L are the domain size and the lamellar thickness of γ phase respectively. The α_2 layer is uniform without domain structures, and of thickness λ_{α_2}. The domains are color–coded for ease of visualization.

Due to tetragonality, the γ phase can exist in six different orientation variants as shown in Fig. 3. All the six γ variants fulfil the Blackburn orientation relationship as detailed in Table 1. Since the probability for the formation of each γ variant is the same (Grujicic and Batchu, 2001), equal volume is assigned to each γ variant in the unit cell, consistent with observations by Inui et al. (1992a) and assumption of Cornec et al. (2015). Each γ lamella is composed of several ordered hexagonal–shaped γ domains while the α_2 lamella is uniform without domain structure due to the absence of orientation variants. The γ lamellae contains six distinct γ domains corresponding to the orientation variants. The hexagonal domains are connected with triple junctions, exhibiting the lattice misorientation. Along X_2–direction, all the six variants

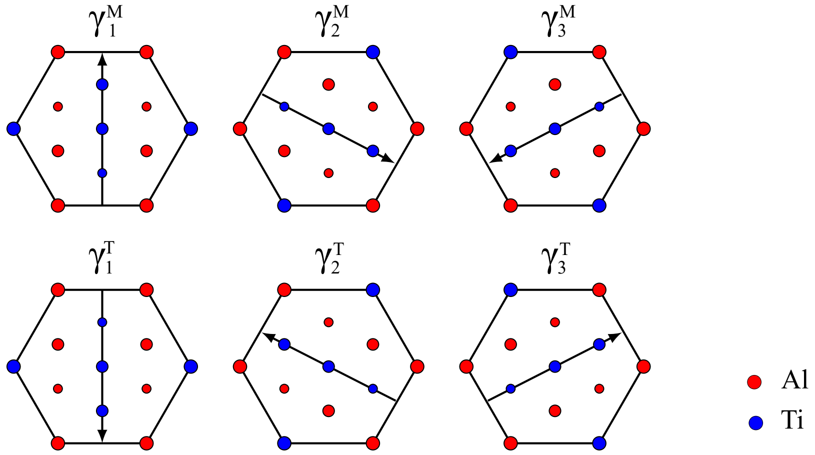

Fig. 3. Six γ orientation variants, where γ_{1-3}^M denotes matrix orientations and γ_{1-3}^T denotes the corresponding twin orientations. The reduced-size circles denote atoms in the plane below. This figure is inspired by Werwer and Cornec (2000).

Table 1. Blackburn orientation relations between γ and α_2 variants.

Variant	**Slip direction**	**Plane normal**
α_2	$[11\bar{2}0]$	(0001)
γ_1^M	$[1\bar{1}0]$	(111)
γ_1^T	$[\bar{1}10]$	(111)
γ_2^M	$[01\bar{1}]$	(111)
γ_2^T	$[0\bar{1}1]$	(111)
γ_3^M	$[\bar{1}01]$	(111)
γ_3^T	$[10\bar{1}]$	(111)

separated by lamellar interfaces are included in each column, for example, the second column at X_1–X_2 plane along X_1–direction, the bottom-up layout is γ_1^M, γ_1^T, γ_2^M, γ_2^T, γ_3^M and γ_3^T.

As shown in Fig. 2, λ_D denotes the average size of γ domain; it is defined as the longest diagonal length in the domain. λ_L and λ_{α_2} represent the average thicknesses of the γ lamellae and the α_2 lamella respectively. These three length scales determine the dimensions of the unit cell

$$L_1 = \frac{3\sqrt{3}}{4}\lambda_D, \quad L_2 = \frac{1}{2}(\lambda_{\alpha_2} + 6\lambda_L), \quad L_3 = \frac{3}{4}\lambda_D. \tag{1}$$

The three lengths, λ_D, λ_L and λ_{α_2} define two dimensionless geometric parameters: the domain aspect ratio λ_D/λ_L, and the initial volume fraction of the α_2 phase, f_{α_2}. The two dimensionless parameters of λ_D/λ_L and f_{α_2} facilitate the studies of scale and *compositional* effects respectively. The initial volume fraction f_{α_2} is determined by the thickness of α_2 phase, λ_{α_2}, as follows

$$f_{\alpha_2} = \frac{\lambda_{\alpha_2}}{\lambda_{\alpha_2} + 6\lambda_L} \tag{2}$$

where λ_L and λ_D are kept constant when f_{α_2} varies. This operation ensures a constant λ_D/λ_L when investigating the effects of f_{α_2}.

Because of various γ orientation variants, the boundaries between γ/γ can be categorized into three types, namely pseudo-twin (PT), ordered-variant (OV) and true-twin (TT) boundaries

(Zhang et al., 2020; Ding et al., 2020):

- PT boundary is that between γ_1^M and γ_2^T, γ_1^M and γ_3^T, γ_2^M and γ_1^T, γ_2^M and γ_3^T, γ_3^M and γ_1^T, γ_3^M and γ_2^T with a rotation angle of 60°,
- OV boundary is that between γ_1^M and γ_2^M, γ_1^M and γ_3^M, γ_2^M and γ_3^M, γ_1^T and γ_3^T, γ_1^T and γ_2^T, γ_2^T and γ_3^T with a rotation angle of 120°,
- TT boundary is that between γ_1^M and γ_1^T, γ_2^M and γ_2^T, γ_3^M and γ_3^T with a rotation angle of 180°.

Werwer and Cornec (2006) have employed two RVEs in their study of the role of superdislocations for modeling plastic deformation of lamellar TiAl, one that incorporates PT boundary while the other OV and TT boundaries/interfces. Cornec et al. (2015) have proposed several types of Periodic Unit Cell (PUC) each containing different arrangments of RVE, with each RVE representing a lamellar phase ($\alpha_2 + \gamma$), and have considered PT, PT and TT, OV and TT boundaries separately in the PUCs.

In this work, all of the γ/γ interfaces have been considered in the RVE under study. Three different variants of $\gamma_1^M, \gamma_2^M, \gamma_3^M$ or $\gamma_1^T, \gamma_2^T, \gamma_3^T$ are considered in the interfaces between neighboring γ lamellae (γ/γ lamella boundaries), while OV boundaries are considered in the interfaces between domains within each γ lamella (γ/γ domain boundaries)

2.2. Deformation systems

Deformation systems in single phases can be grouped either by their deformation mechanism (e.g. ordinary slip, super slip and twinning in γ-TiAl phase) or by crystallographically equivalent slip planes (e.g. basal, prismatic and pyramidal slips in α_2-Ti_3Al phase). Due to the fact that $(111)_\gamma$ plane of all γ domains and the $(0001)_{\alpha_2}$ plane of all α_2 lamellae are always co–planar to the lamella interfaces, the slip systems can also be classified as transversal, longitudinal and mixed based on morphological deformation modes (Lebensohn et al., 1998; Grujicic and Batchu, 2001; Schnabel, 2018). These morphological deformation modes can be distinguished according to the following features:

- Transversal: slip direction inclined to lamellae, plane normal inclined to lamellae.
- Longitudinal: slip direction parallel to lamellae, plane normal perpendicular to lamellae
- Mixed: slip direction parallel to lamellae, plane normal inclined to lamellae.

In general, two principal deformation modes can be identified in PST crystals based on activation of deformation systems on crystallographic planes; hard and soft modes (Fujiwara et al., 1990; Hazzledine and Kad, 1995; You et al., 2013). In hard mode, shear deformations occur across lamella interfaces (mixed and transversal systems) where lamellar thickness plays a dominant role, whereas in soft mode the shear deformations occur along lamella interfaces/domain boundaries (longitudinal systems) where domain size plays a dominant role (Inui et al., 1992a; Hazzledine and Kad, 1995; Kad et al., 1995; Umeda et al., 1997; You et al., 2013; Palomares-García et al., 2017) In view that twinning is a potential plastic deformation mechanism at low temperatures and high strain rates, it is pertinent to consider only slips for bending at high temperature and low strain rate. This strategy has been adopted by others (e.g., Grujicic and Batchu, 2001; Grujicic et al., 2003a).

Table 2. Slip systems in tetragonal γ-TiAl and hexagonal α_2-Ti$_3$Al phases with mechanism classification. Note that Miller index and Miller-Bravais index are used for γ-TiAl and α_2-Ti$_3$Al phases, respectively (Schnabel, 2018).

Phase	System	Mechanism	Morphology
γ-TiAl	$1/2[1\bar{1}0](111)$	Ordinary slip	Longitudinal
	$[01\bar{1}](111)$	Super slip	Longitudinal
	$[10\bar{1}](111)$	Super slip	Longitudinal
	$1/2[1\bar{1}0](\bar{1}\bar{1}1)$	Ordinary slip	Mixed
	$[01\bar{1}](\bar{1}11)$	Super slip	Mixed
	$[10\bar{1}](1\bar{1}1)$	Super slip	Mixed
	$1/2[110](1\bar{1}1)$	Ordinary slip	Transversal
	$1/2[\bar{1}\bar{1}0](\bar{1}11)$	Ordinary slip	Transversal
	$[0\bar{1}\bar{1}](\bar{1}\bar{1}1)$	Super slip	Transversal
	$[\bar{1}0\bar{1}](\bar{1}\bar{1}1)$	Super slip	Transversal
	$[0\bar{1}\bar{1}](1\bar{1}1)$	Super slip	Transversal
	$[\bar{1}0\bar{1}](\bar{1}11)$	Super slip	Transversal
α_2-Ti$_3$Al	$\{0001\}\langle 11\bar{2}0\rangle$	Basal slip	Longitudinal
	$\{1\bar{1}00\}\langle 11\bar{2}0\rangle$	Prismatic slip	Mixed
	$\{11\bar{2}1\}\langle 11\bar{2}6\rangle$	Pyramidal slip	Transversal

2.3. Crystal plasticity model

The crystal plasticity constitutive model employed in this study is formulated based on the work of Hill and Rice (1972); Hutchinson (1976); Asaro and Rice (1977); Kothari (1997). For completeness of this paper, a brief introduction of the model is provided here.

The total deformation gradient can be multiplicatively decomposed as

$$\boldsymbol{F} = \boldsymbol{F}^e \boldsymbol{F}^p \tag{3}$$

where $\boldsymbol{F}^e$ is the elastic deformation gradient denoting the elastic distortion and rotation of the lattice, where $\boldsymbol{F}^e \equiv \boldsymbol{F}\boldsymbol{F}^{p-1}$, and $\boldsymbol{F}^p$ the plastic deformation gradient characterizing the shear strain on the active slip systems. Within the finite strain setting, the Hook's law is formulated in the rate form as

$$\overset{\nabla}{\boldsymbol{\tau}} = \mathcal{L} : \boldsymbol{D}^e \tag{4}$$

where $\overset{\nabla}{\boldsymbol{\tau}} = \dot{\boldsymbol{\tau}} - \boldsymbol{W}^e \boldsymbol{\tau} + \boldsymbol{\tau} \boldsymbol{W}^e$ is the Jaumann rate of the Kirchhoff stress $\boldsymbol{\tau}$, $\mathcal{L}$ the rank-4 elasticity tensor, $\boldsymbol{D}^e$ and $\boldsymbol{W}^e$ are the elastic deformation rate and spin tensor

$$\boldsymbol{D}^e = \mathrm{sym}\left(\dot{\boldsymbol{F}}^e \boldsymbol{F}^{e-1}\right), \quad \boldsymbol{W}^e = \mathrm{skw}\left(\dot{\boldsymbol{F}}^e \boldsymbol{F}^{e-1}\right). \tag{5}$$

Using Voigt notation, $\mathcal{L}$ has been defined in Appendix A, in terms of the elastic stiffness matrix for tetragonal crystal γ-TiAl and hexagonal crystal α_2-Ti$_3$Al, respectively.

The change of $\boldsymbol{F}^p$, describing the evolution of plastic deformation gradient, is represented by

$$\dot{\boldsymbol{F}}^p \boldsymbol{F}^{p-1} = \sum_{\alpha} \dot{\gamma}^{(\alpha)} \boldsymbol{s}^{(\alpha)} \otimes \boldsymbol{m}^{(\alpha)} \tag{6}$$

where $\dot{\gamma}^{(\alpha)}$ is the plastic shearing rate, $\boldsymbol{s}^{(\alpha)}$ a unit slip direction and $\boldsymbol{m}^{(\alpha)}$ orthonormal to the slip plane in the reference plane.

The plastic shearing rate $\dot{\gamma}^{(\alpha)}$ of the αth slip system is determined by the simple power law as (Hutchinson, 1976)

$$\dot{\gamma}^{(\alpha)} = \dot{\gamma}_0 \left| \frac{\tau^{(\alpha)}}{\tau_c{}^{(\alpha)}} \right|^m \operatorname{sgn}(\tau^{(\alpha)}) \tag{7}$$

where $\tau^{(\alpha)} = \boldsymbol{\tau} : \boldsymbol{s}^{(\alpha)} \otimes \boldsymbol{m}^{(\alpha)}$ is the resolved shear stress, $\tau_c{}^{(\alpha)}$ the critical resolved shear stress (representative of slip resistance) of the αth slip system, $\dot{\gamma}_0$ the reference strain rate, and m the power exponent of rate sensitivity. In this formulation, $\dot{\gamma}_0$ and m are assumed to be identical for all slip systems in either of the crystals.

The evolution of the deformation resistance on the αth slip system characterizes the strain hardening behavior via the incremental relation, given by (Kothari, 1997)

$$\dot{\tau_c}{}^{(\alpha)} = \sum_{\beta} h_{\alpha\beta} \left| \dot{\gamma}^{(\beta)} \right| \tag{8}$$

where $h_{\alpha\beta}$ are the strain hardening moduli, accounting for the contributions from all the active slip systems. $h_{\alpha\beta}$ encompasses the self-hardening moduli where $\alpha = \beta$ and latent hardening moduli where $\alpha \neq \beta$. Given the quantity of the slip systems of the two phases, the complete matrix of the hardening moduli $h_{\alpha\beta}$ manifests descriptive intractability. For instance, there are 12 slip systems for γ-TiAl phase such that $h_{\alpha\beta}$ is 12×12 matrix of 144 entries. $h_{\alpha\beta}$ of α_2-Ti_3Al phase shares the same dimension as that of γ-TiAl phase. For the sake of brevity and clarity, $h_{\alpha\beta}$ is simplified as

$$h_{\alpha\beta} = q_{\alpha\beta} h^{(\beta)}. \tag{9}$$

The parameter $q_{\alpha\beta}$ is a measure for latent hardening

$$q_{\alpha\beta} = \begin{cases} 1 & \text{for coplanar slip systems } \alpha \text{ and } \beta \\ q_l & \text{otherwise} \end{cases} \tag{10}$$

where q_l takes the value 1.4, following Kad et al. (1995); Grujicic and Batchu (2001).

The self hardening is expressed following Kothari (1997) as

$$h^{(\beta)} = h_0^{(\beta)} \left| 1 - \frac{\tau_c{}^{(\beta)}}{\tau_s^{(\beta)}} \right|^{n^{(\beta)}} \operatorname{sgn}\left(1 - \frac{\tau_c{}^{(\beta)}}{\tau_s^{(\beta)}} \right) \tag{11}$$

where $h_0^{(\beta)}$ is the initial hardening modulus, $n^{(\beta)}$ the hardening exponent and $\tau_s^{(\beta)}$ the saturation slip resistance.

The crystal plasticity model parameters utilized in this work for γ-TiAl and α_2-Ti_3Al phases are listed in Table 3 and Table 4 respectively. These parameters are widely adopted and are extracted from Fu and Yoo (1990); Yoo et al. (1995); Kad et al. (1995); Grujicic and Batchu (2001).

2.4. Numerical implementation

This subsection details the boundary and loading conditions to be imposed on the 3D unit cell. The cell is initially at rest, and rotation–controlled displacements are applied on X_2-X_3 planes at two ends of the cell, $X_1 = \pm L_1$, to trigger equal and opposite rotations. Roller constraints are imposed on X_1-X_2 planes at the two surfaces, $X_3 = \pm L_3$, along the X_3 direction (i.e. the plane strain conditions for bending). Denoting u_i ($i = 1, 2, 3$) as the three–dimensional displacements of a material point (X_1, X_2, X_3), the displacement boundary conditions are given by

Table 3. Crystal plasticity model parameters for γ-TiAl phase

Parameter		**Value**	**Reference**
Elastic matrix, C_{11}		190 GPa	Fu and Yoo (1990)
Elastic matrix, C_{12}		105 GPa	Fu and Yoo (1990)
Elastic matrix, C_{13}		90 GPa	Fu and Yoo (1990)
Elastic matrix, C_{33}		185 GPa	Fu and Yoo (1990)
Elastic matrix, C_{44}		120 GPa	Fu and Yoo (1990)
Elastic matrix, C_{66}		50 GPa	Fu and Yoo (1990)
Reference shearing rate, $\dot{\gamma}_0$		0.001 s^{-1}	Kad et al. (1995)
Rate sensitivity exponent, m		40	This work
Self-hardening exponent, n	$\{111\}\langle 1\bar{1}0]$	3.1	Grujicic and Batchu (2001)
	$\{111\}\langle \bar{1}01]$	3.0	Grujicic and Batchu (2001)
Self-hardening modulus, h_0	$\{111\}\langle 1\bar{1}0]$	940.2 MPa	Grujicic and Batchu (2001)
	$\{111\}\langle \bar{1}01]$	950.7 MPa	Grujicic and Batchu (2001)
Initial slip resistance, τ_0	$\{111\}\langle 1\bar{1}0]$	14.3 MPa	Grujicic and Batchu (2001)
	$\{111\}\langle \bar{1}01]$	22.7 MPa	Grujicic and Batchu (2001)
Saturation slip resistance, τ_s	$\{111\}\langle 1\bar{1}0]$	212.2 MPa	Grujicic and Batchu (2001)
	$\{111\}\langle \bar{1}01]$	291.1 MPa	Grujicic and Batchu (2001)

- At $X_1 = \pm L_1$

$$\begin{pmatrix} u_1 \\ u_2 \end{pmatrix} = \begin{pmatrix} \cos\phi & \pm\sin\phi \\ \mp\sin\phi & \cos\phi \end{pmatrix} \begin{pmatrix} X_1 \\ X_2 + Y_0 \end{pmatrix} - \begin{pmatrix} X_1 \\ X_2 + Y_0 \end{pmatrix} \tag{12}$$

- At $X_3 = \pm L_3$

$$u_3 = 0 \tag{13}$$

In the above, ϕ is the rotation or bending angle at both ends of unit cell at $X_1 = \pm L_1$ with respect to X_3 axis. It is taken to be positive counterclockwise and negative clockwise, and Y_0 is the center of the curvature during the course of the bending deformation. The remaining degrees of freedom (DOFs) are kept free, implying zero (anti-periodic) tractions. It should be noted that the two–parameter bending mode (12) is similar to that employed by Du et al. (2020) for plane strain bending of an elastomeric rectangular block (see (17) therein).

The boundary conditions are imposed through multi-point constraints *via* the user subroutine *MPC. A dummy node with DOFs ϕ and Y_0 is introduced to establish master–slave relations in the boundary conditions (12) (Cheng and Guo, 2007; Wong and Guo, 2015; Liu et al., 2016; Guo and Wong, 2018). Clearly, ϕ is work–conjugate with bending moment M while Y_0 is a supplementary kinematic variable used to minimize the energy of the system with a zero nodal force. There exists a total virtual work equivalence between the dummy node and the 3D unit cell; namely,the total internal virtual work is equal to the external virtual work

$$\int_V \boldsymbol{P} : \delta \boldsymbol{F} dV = 2M\delta\phi = 2ML_1\delta\kappa \tag{14}$$

where $\boldsymbol{P}$ is the first Piola-Kirchholf stress, V the cell volume in the undeformed reference configuration,

$$M = \int_{X_1 = L_1} (x_2 P_{11} - x_1 P_{21})\, dS \tag{15}$$

Table 4. Crystal plasticity model parameters for α_2-Ti_3Al phase

Parameter		**Value**	**Reference**
Elastic matrix, C_{11}		221 GPa	Yoo et al. (1995)
Elastic matrix, C_{12}		71 GPa	Yoo et al. (1995)
Elastic matrix, C_{13}		85 GPa	Yoo et al. (1995)
Elastic matrix, C_{33}		238 GPa	Yoo et al. (1995)
Elastic matrix, C_{44}		69 GPa	Yoo et al. (1995)
Reference shearing rate, $\dot{\gamma}_0$		0.001 s^{-1}	Kad et al. (1995)
Rate sensitivity exponent, m		40	This work
Self-hardening exponent, n	$\{0001\}\langle 11\bar{2}0\rangle$	3.0	Grujicic and Batchu (2001)
	$\{1\bar{1}00\}\langle 11\bar{2}0\rangle$	2.7	Grujicic and Batchu (2001)
	$\{11\bar{2}1\}\langle 11\bar{2}6\rangle$	2.9	Grujicic and Batchu (2001)
Self-hardening modulus, h_0	$\{0001\}\langle 11\bar{2}0\rangle$	742.8 MPa	Grujicic and Batchu (2001)
	$\{1\bar{1}00\}\langle 11\bar{2}0\rangle$	861.7 MPa	Grujicic and Batchu (2001)
	$\{11\bar{2}1\}\langle 11\bar{2}6\rangle$	814.7 MPa	Grujicic and Batchu (2001)
Initial slip resistance, τ_0	$\{0001\}\langle 11\bar{2}0\rangle$	44.8 MPa	Grujicic and Batchu (2001)
	$\{1\bar{1}00\}\langle 11\bar{2}0\rangle$	19.2 MPa	Grujicic and Batchu (2001)
	$\{11\bar{2}1\}\langle 11\bar{2}6\rangle$	121.9 MPa	Grujicic and Batchu (2001)
Saturation slip resistance, τ_s	$\{0001\}\langle 11\bar{2}0\rangle$	417.7 MPa	Grujicic and Batchu (2001)
	$\{1\bar{1}00\}\langle 11\bar{2}0\rangle$	148.3 MPa	Grujicic and Batchu (2001)
	$\{11\bar{2}1\}\langle 11\bar{2}6\rangle$	1586.3 MPa	Grujicic and Batchu (2001)

$\tau_s^* = 1586.3$ MPa is used for the bending moment normalization.

the bending moment (see Appendix B for the calculation of bending moment), and $\kappa = \phi/L_1$ the overall curvature. In (15), (x_1, x_2) is the *current* position from the center of curvature.

The second moment of the cross–sectional area at $X_1 = L_1$ is

$$I = \tfrac{4}{3}{L_2}^3 L_3. \tag{16}$$

With reference to small strain beam theory for isotropic materials with Young's modulus E, bending moment has a linear relationship with the curvature: $M = EI\kappa$. For the nonlinear bending problem under study, it is convenient to normalize the bending moment as $ML_1/\tau_s^* I$, where $\tau_s^* = 1586.3$ MPa is the saturation slip resistance of pyramidal slip systems as presented in Table 4. In noting from (15) that the bending moment M is a function of cross–sectional area $(L_2 \times L_3)$, the rationale for the normalization of M with I is to essentially isolate the effects of cross–sectional area in the preceding analyses on scale and geometric effects, i.e. lamella's domain size aspect ratio and volume fraction, and configurational variation of lamellae. This will be apparent in the presentation of results in Section 3. Given the material properties in Table 3 and Table 4, the dimensionless bending moment is a nonlinear function of the bending angle ϕ and the geometric parameters – the domain aspect ratio λ_D/λ_L and the initial volume fraction of the α_2 phase:

$$\frac{M}{\tau_s^* V} = \mathcal{F}\left(\phi; \frac{\lambda_D}{\lambda_L}, f_{\alpha_2}\right). \tag{17}$$

The foregoing crystal plasticity model is implemented into the general-purpose finite ele-

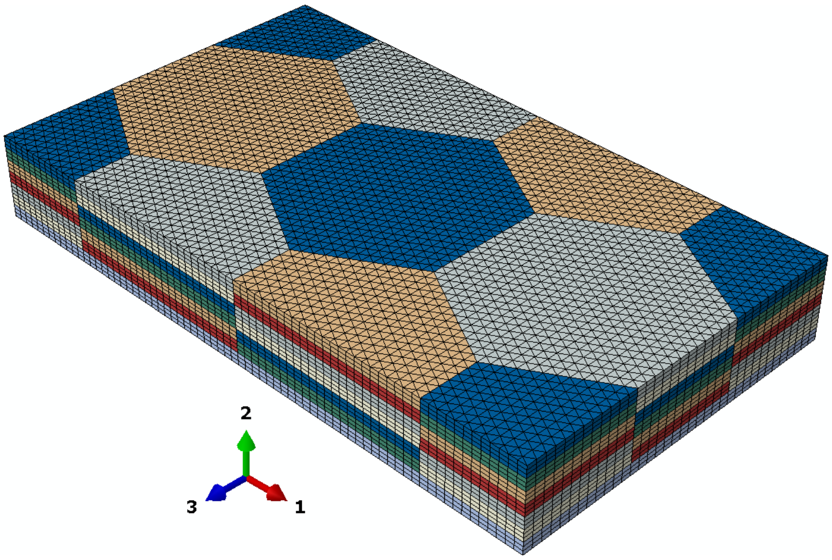

Fig. 4. An example finite element mesh for $\lambda_D/\lambda_L = 20$ and $f_{\alpha_2} = 15\%$.

ment program ABAQUS *via* UMAT, the user–subroutine for defining the mechanical constitutive behavior of PST lamellar TiAl crystal. Fig. 4 shows an example of the finite element mesh for $\lambda_D/\lambda_L = 20$ and $f_{\alpha_2} = 15\%$, where the RVE with $\alpha_2 + 6\gamma$ substructures in Fig. 2 is discretized into three–dimensional 6–node linear triangular prisms, hybrid with constant pressure (C3D6H). The total number of elements is 110, 376 with 60, 215 nodes.

3. Results and discussion

This section presents the results of the micromechanial analyses on the bending of PST single crystal of TiAl. The results focus on its bending responses under the influences of domain size aspect ratio λ_D/λ_L, volume fraction of α_2 phase f_{α_2} and the boundary constraints imposed on the RVE. The dependent variables that will be presented in the subsequent subsections, primarily bending moments and stresses, represent the overall response of the RVE and they take on dimensionless normalized forms. Henceforth, the terms ”bending moment”, ”tensile stress” and ”compressive stress” shall refer to their normalized forms, unless otherwise stated.

3.1. Shear strain discontinuities

Sagging and hogging are terms used in solid mechanics and structural and civil engineering to describe the shape that a beam or similar long slender object will deform under loads; sagging describes a beam that curves downwards in its middle, while hogging describes a beam that curves upwards. The bending moments associated with sagging and hogging are known as sagging and hogging moments respectively. Sagging and hogging moments correspond to negative and positive bending angles ϕ respectively. Fig. 5 displays the contour plots of discontinuities in cumulative shear strain, and examplifying the sagging and hogging shapes in a lamellar PST TiAl of $\lambda_D/\lambda_L = 20$ and $f_{\alpha_2} = 15\%$ subjected to bending angles $|\phi| = 0.002$, 0.1 and 0.5 rad.

The total cumulative shear strain γ_c on all active slip systems characterizes the activation of

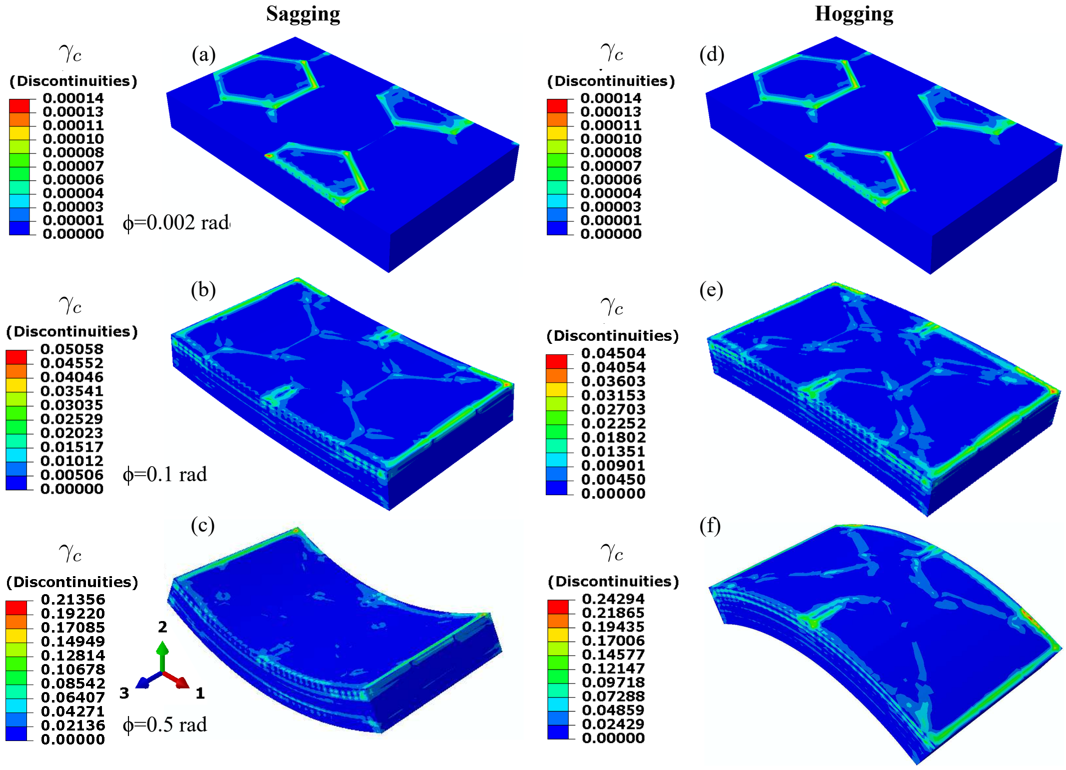

Fig. 5. Contour plots of discontinuities in cumulative shear strain γ_c in lamellar PST TiAl at various bending angles ϕ where $\lambda_D/\lambda_L = 20$ and $f_{\alpha_2} = 15\%$, examplifying (a)-(c) sagging and (d)-(f) hogging shapes. Discontinuities occur in domain boundaries within the lamellae and lamella boundaries.

slip systems, and is expressed as

$$\gamma_c = \sum_{\alpha} \int \left| \dot{\gamma}^{(\alpha)} \right| dt \tag{18}$$

The discontinuities in γ_c represent the maximum differences in the computed γ_c between adjacent elements (ABAQUS Version 6.14); they highlight the local strain gradients that develop in the heterogeneous microstructure during the bending process. At first glance, it can be observed that the patterns of localized strain gradients are almost similar under sagging and hogging moments, though it is not as apparent for the case of $\phi = \pm 0.5$ rad due to the the chosen limits of the contour plot for sagging. It can also be observed that the localized strain gradients are confined within the lamella at γ domain boundaries at low bending angle i.e. $\gamma = 0.002$ rad. As bending angle increases, strain gradients develop across γ/γ lamellae boundaries and α_2/γ lamellae boundary. The discontinuities or strain localizations appearing along the edges of the RVE are due to the effects of the imposed boundary conditions. The strain localization arises from the microstructural inhomogeneity such as phase incompatibility, orientation variants (Kad et al., 1995; Antolovich and Armstrong, 2014), and as a consequence of crystallographic slips (Harren and Asaro, 1989). The domains or lamellae accommodate each other to avert discontinuity through slip motion and storage at the boundaries, and the accommodation of slips among neighboring domains or lamellae causes the strain localization at the boundaries (Fleck et al., 1994; Qiu et al., 2020). The presence of strain localization across the boundaries infers the activation of hard mode slips (Kad et al., 1995); all the slip systems are transversal under both sagging and hogging moments. Indeed, numerical results of Fig. 5 for $\lambda_D/\lambda_L = 20$ and $f_{\alpha 2} = 15\%$ indicate that two ordinary, four super and two pyramidal slip systems are activated under sagging moments, while two ordinary, one super and two pyramidal are operative under hogging moments.

Remark: Incompatible deformations and stress concentrations between distinct γ–domains are significant due to elastic misorientation therein when the bending angle is small. With the increase of bending angle, however, the deformation becomes relatively compatible and the stress concentration at triple junctions is retrieved.

3.2. Domain aspect ratio, λ_D/λ_L

The effects of domain aspect ratio λ_D/λ_L on bending are presented in this section, where the length scales λ_D and λ_L are the domain size and lamella thickness respectively, as defined previously. Domain sizes have been observed to vary from 100 nm to 500 µm (Inui et al., 1992b; Nakano et al., 1992; Dimiduk et al., 1998; Maziasz and Liu, 1998) , while the lamellar thicknesses may range from tens of nanometre to a few hundreds of micrometre (Kim, 1998; Maziasz and Liu, 1998; Zhu et al., 2006; Werwer et al., 2007) . In this work, λ_D is held constant while λ_L is varied accordingly for the domain aspect ratios under consideration, namely λ_D/λ_L = 10, 20 and 40. Indeed, many well–documented studies on dominant size effects in relation to PST TiAl have reported that λ_L plays a dominant role when hard mode operates (e.g., Inui et al., 1992a; Hazzledine and Kad, 1995; Kad et al., 1995; Umeda et al., 1997). Hard mode is expected to be the dominant during bending where the active slip systems are mixed and transversal. The volume fraction of α_2 phase, f_{α_2}, is maintained at 15%, unless otherwise stated.

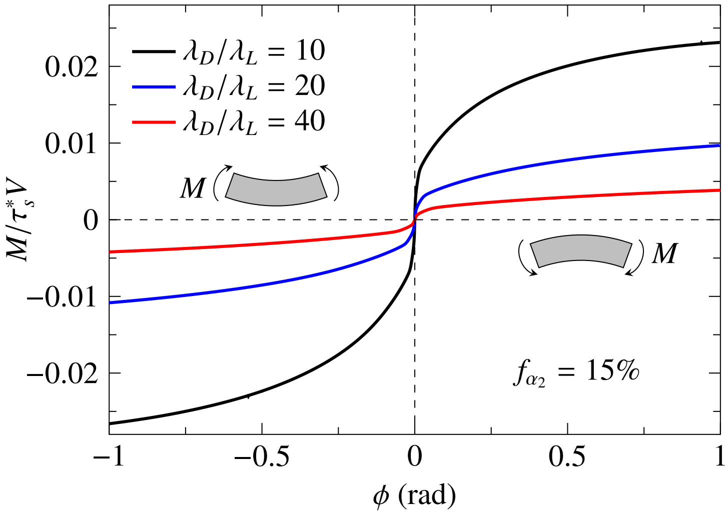

Fig. 6. Variation of bending moment $M/\tau_s^* V$ with bending angle ϕ for three levels of domain size aspect ratio $\lambda_D/\lambda_L = 10, 20$ and 40, with f_{α_2} = 15%. Hogging and sagging moments are represented by positive and negative ϕ respectively.

Fig. 6 depicts the overall bending response of the PST TiAl lamellae for three levels of domain size aspect ratio λ_D/λ_L considered. Positive ϕ corresponds to the case of the lamellae subjected to hogging moments ($+M$) while negative ϕ to sagging moments ($-M$). It can be observed that bending moment decreases as domain aspect ratio λ_D/λ_L increases. With λ_D being held constant, a decrease in γ lamella thickness λ_L implies an increase in λ_D/λ_L. In other words, a thinner lamella induces a lower bending moment, an observation that can be elucidated from geometrical and kinematics considerations. Recall from (1) the relations between the three lengths describing the sizes of γ and α_2 lamellae (λ_D, λ_L and λ_{α_2}) and the dimensions of the unit cell (L_1, L_2 and L_3), the overall thickness of the unit cell L_2 increases as λ_L increases and vice versa, with L_1 and L_3 remaining constant for prescribed λ_D and λ_{α_2}. With that, it can be seen from (16) that the second moment of cross-sectional area I scales with L_2 raised to its third power. As a consequence and from beam theory, bending moment M therefore increases with λ_L since $M \propto I$. It is also observed from the figure that the the non–linear relationship between the induced bending moment and bending angle becomes more pronounced at large ϕ as λ_D/λ_L decreases. A closer inspection of the figure reveals presence of linear response of M/τ_s^*V at low bending angles ϕ. This is exemplified in Fig. 7, where the overall bending response of the cell is plotted in the domain $-0.015 \leq \phi \leq 0.015$, for the same levels of domain aspect ratio λ_D/λ_L considered. As in Fig. 6, positive M/τ_s^*V corresponds to the case of hogging while negative sagging. From Fig. 7, linear relationships between bending moment and bending angle are clearly evident for both hogging and sagging at low ϕ, with the respective elastic slopes denoted by dashed lines. As ϕ is further increased, the curves of M/τ_s^*V versus ϕ begin to deviate from the linear elastic slopes.

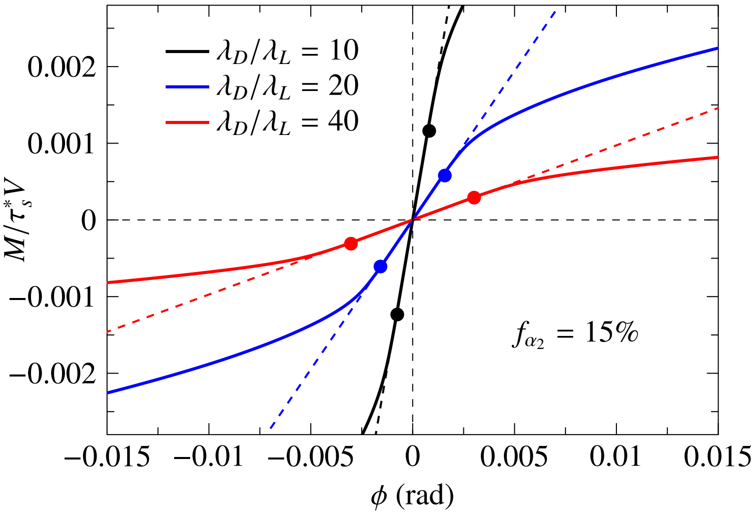

Fig. 7. Linear relationship between M/τ_s^*V and ϕ at low bending angles, for the three levels of λ_D/λ_L. Solid circles mark the moment at initial yield of the overall cell response. Dashed lines represent the respective elastic slopes.

It is known from classical beam theory that bending moment–rotation relation is related to tensile stress–strain relation, though this relationship is not straightforward in the context of discrete dislocation due to the various dislocation structures that evolve (Cleveringa et al., 1999). Assuming the linear regime corresponds to the elastic response, we can then define the point at which deviation from the linear slope occurs as the initial yield. This is the elastic limit and are shown as marked by the solid circles in Fig. 7, and it indicates the first occurrence of dislocation activities, and in the context of CPFEM slip activities. In this work, the point defining the elastic limit is such that its gradient with respect to the origin deviates from the elastic slope by 0.02%. The bending moment at which initial yield occurs is herein denoted by (M_Y/τ_s^*V) and the bending angle at which it occurs as ϕ_Y. It is observed that the magnitude (M_Y/τ_s^*V) increases and the corresponding ϕ_Y decreases, as λ_D/λ_L decreases. In other words, the initial yield and the corresponding (M_Y/τ_s^*V) increases as thickness of γ lamallae increases i.e. as λ_L increases. At the same time, the increase in λ_L also has an effect of "hastening" the onset of initial yield; its occurrence at a lower bending angle. From the perspectives of dislocations and slips, we can rationalize this observation by realizing that there is a maximum number of dislocations that can be accomodated on any slip plane due to the spacings of dislocations in the pile up. It can be envisioned that the maximum number of dislocations per slip plane increases with the size of the unit cell or in general the specimen; in this case thicknesses of the γ lamallae and consequently the cell's thickness L_2. According to Fleck et al. (1994), the total density of dislocations determines material hardening, and their origins due to strain gradient which, in this context, is a result of loading geometry i.e. bending.

From small strain beam theory, we can approximate the bending stress in the linear elastic regime *via* $\sigma_b = My/I$, where σ_b is the bending stress, y the distance from the neutral axis or neutral plane, with M, V and I as defined previously. In the elastic limit and from the bending stress relation, we can write

$$\frac{\sigma_Y}{\tau_s^*} = \left(\frac{M_Y}{\tau_s^* V}\right)\left(\frac{yV}{I}\right), \tag{19}$$

where σ_Y/τ_s^* is the overall initial yield stress, $(M_Y/\tau_s V)$ the overall moment at initial yield that can be obtained from Fig. 7. The neutral axis needs to be computed for the evaluation of y. In considering the $\alpha + 6\gamma$ TiAl to be a composite beam and using the method of transformed section, the location of the equivalent neutral axis $\bar{y}$ relative to the bottommost surface of α lamellae (see Fig. 2) i.e. at $X_2 = -L_2$ can be evaluated using

$$\bar{y} = \frac{\Sigma A_i^{\gamma} \bar{y}_i^{\gamma} + n_m A^{\alpha} \bar{y}^{\alpha}}{\Sigma A_i^{\gamma} + n_m A^{\alpha}}, \tag{20}$$

where A_i^{γ} $(i = 1, 2, ...6)$ refers to the cross–sectional area of i^{th} γ lamella in the $X_2 - X_3$ plane, A^{α} the cross–sectional area of α lamellae, $\bar{y}_i^{\gamma}$ and $\bar{y}^{\alpha}$ the locations of neutral axes of the respective lamellae and n_m the modular ratio, defined as $n_m = C_{11}^{\alpha}/C_{11}^{\gamma}$ with C_{11} the elastic constants from Table 3 and Table 4. Here, we have taken y to be positive in the positive X_2–direction (above the neutral axis $\bar{y}$) and vice versa. Thus it is trivial to note from (19) that maximum normal tensile stress $(\sigma_Y/\tau_s^*)_t$ will occur at $y = +L_2$ while minimum normal compressive stress $(\sigma_Y/\tau_s^*)_c$ at $y = -L_2$ under hogging moments respectively). Similarly, $(\sigma_Y/\tau_s^*)_c$ will occur at $y = +L_2$ while $(\sigma_Y/\tau_s^*)_t$ at $y = -L_2$ under sagging moments respectively). Table 5 lists the computed values at initial yield for the bending moment $(M_Y/\tau_s^* V)$, tensile stress $(\sigma_Y/\tau_s^*)_t$ and compressive stress $(\sigma_Y/\tau_s^*)_c$ under hogging and sagging moments for three levels of λ_D/λ_L and $f_{\alpha_2} = 15\%$. It can be noticed from the table that both maximum tensile and compressive yield

Table 5. List of values for bending angle, bending moment, tensile and compressive stresses at initial yield under both hogging and sagging moments for $\lambda_D/\lambda_L = 10, 20, 40$ and $f_{\alpha_2} = 15\%$.

Moment	λ_D/λ_L	ϕ_Y	$\left(\frac{M_Y}{\tau_s^* V}\right)$	$\left(\frac{\sigma_Y}{\tau_s^*}\right)_t$	$\left(\frac{\sigma_Y}{\tau_s^*}\right)_c$
Hogging	10	8.23×10^{-4}	1.28×10^{-3}	0.0144	-0.0140
	20	1.61×10^{-3}	6.25×10^{-4}	0.0140	-0.0136
	40	3.21×10^{-3}	3.04×10^{-4}	0.0136	-0.0132
Sagging	10	-8.29×10^{-4}	-1.29×10^{-3}	0.0141	-0.0145
	20	-1.61×10^{-3}	-6.28×10^{-4}	0.0137	-0.0141
	40	-3.20×10^{-3}	-3.13×10^{-4}	0.0136	-0.0140

stress, $(\sigma_Y/\tau_s^*)_t$ and $(\sigma_Y/\tau_s^*)_c$ respectively, display decreasing trends as λ_D/λ_L increases i.e. as λ_L decreases, though the increments are somewhat marginal. Nevertheless, the observed trend may be attributed to the lower total dislocation density associated with lower λ_L, or thinner γ lamellae. It is interesting to note from Table 5 and Fig. 7 that the onset of slip activities occurs is delayed with larger ϕ_Y as λ_D/λ_L is increased i.e. as λ_L is decreased, as a result of increased compliance of the lamallae to bending.

Re-directing attention back to Fig. 6, it is of interest to note that bending responses is asymmetric under sagging and hogging moments; the magnitudes of $M/\tau_s^* V$ under sagging are larger than those under hogging e.g. comparing $M/\tau_s^* V$ at $\phi = \pm 1$ for $\lambda_D/\lambda_L = 10$. Numerical results reveal two ordinary, four super and two pyramidal slip systems are active under sagging moments, while two ordinary, one super and two pyramidal are active under hogging moments. As slip systems can render resistance to deformations (Chen et al., 2019; Cornec et al., 2015), the presence of three additional super slip systems under sagging is likely to result in higher resistance and hence, larger bending moment.

In view of the overall bending moment reponses in Fig. 6, it is possible to establish a scaling law relating $M/\tau_s^* V$, λ_D/λ_L and ϕ. To this end, the parameter space in Fig. 6 is expanded to include $\lambda_D/\lambda_L = 30$ and 50 and five levels of $\phi = 0.1,\ 0.3,\ 0.5,\ 0.7,\ 0.9$ rad are selected to characterize the initial, intermediate and late stages of bending. Fig. 8 depicts the relationship between bending moment $M/\tau_s^* V$ and domain aspect ratio λ_D/λ_L at the five discrete bending angles of ϕ. Solid circles represent the numerical results while the dashed lines denote fitted scaling laws, obtained *via* least–square fit. It can be readily deduced that proposed scaling law takes the form

$$\frac{|M|}{\tau_s^* V} = a \cdot \left(\frac{\lambda_D}{\lambda_L}\right)^b, \tag{21}$$

where the values of coefficient a and exponent b are listed in Table 6. Here, b is expressed as a function of ϕ ($\phi \neq 0$) and is obtained by least–square fitting in the plot of b versus ϕ. One may

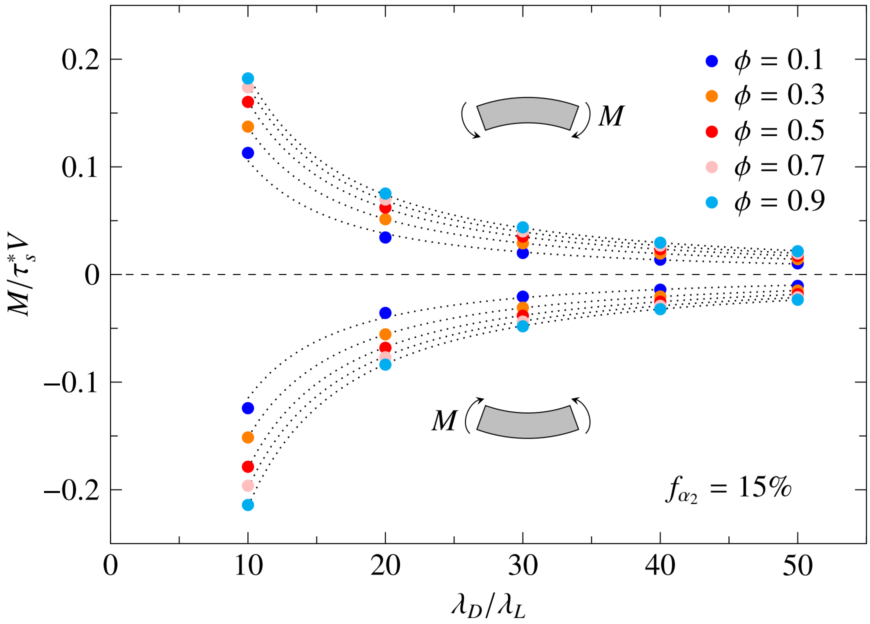

Fig. 8. Relationships between the bending moment $M/\tau_s^* V$ and domain aspect ratio λ_D/λ_L for five levels of bending angles $\phi = 0.1,\ 0.3,\ 0.5,\ 0.7,\ 0.9$ rad under both sagging and hogging moments, with $f_{\alpha_2} = 15\%$. The dotted lines represent the fitted scaling relations.

Table 6. Fitted values of coefficient a and exponent b in the ϕ-dependent scaling law.

Moment	ϕ (rad)	a	b
Hogging	0.1	3.171	0.181ϕ-1.481
	0.3	3.498	
	0.5	3.937	
	0.7	3.990	
	0.9	4.054	
Sagging	0.1	-3.840	0.181ϕ-1.517
	0.3	-4.176	
	0.5	-4.677	
	0.7	-4.797	
	0.9	-5.070	

make use of (21) to estimate the induced bending moment for a prescribed ϕ ($0.1 \leq \phi \leq 0.9$) and λ_D/λ_L. For example when $\lambda_D/\lambda_L = 1$, one can see that $(M/\tau_s^* V) = a$, and a is a constant which depends on ϕ as well as the bending mode i.e. sagging or hogging moments.

3.3. Volume fraction of α_2 phase, f_{α_2}

The effect of volume fraction of the α_2 phase f_{α_2} on the bending behavior of PST TiAl is explored in this subsection. Here, the volume fraction is varied from 5% to 25%, for a fixed domain aspect ratio $\lambda_D/\lambda_L = 20$. Fig. 9 illustrates the variation of the cell's overall bending moment $M/\tau_s^* V$ with bending angle ϕ for three levels of volume fraction of α_2 phase f_{α_2}, with $\lambda_D/\lambda_L = 20$. The trend of increasing $M/\tau_s^* V$ with f_{α_2} can be observed under both hogging and sagging moments. From (1) and (16), increasing f_{α_2} essentially increases the cell's dimension L_2, its second moment of area I as well as increased accommodation of dislocations per slip plane, thereby leading to the observed trend. With α_2 phase being considerably harder than the

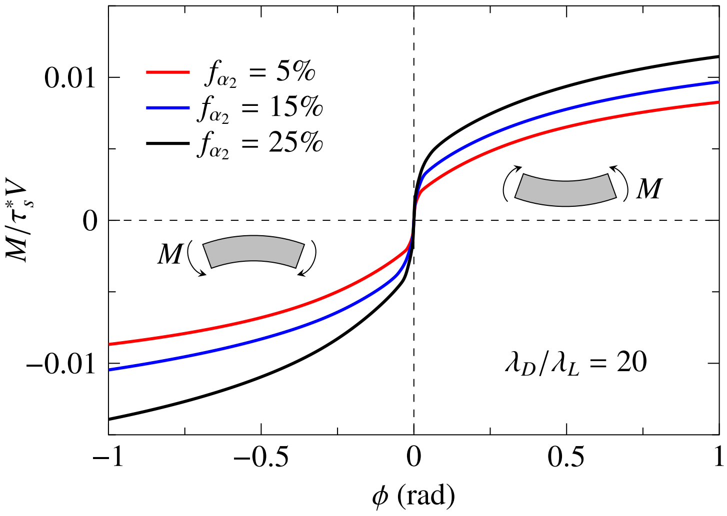

Fig. 9. Variation of bending moment $ML_1/\tau_s^* V$ with bending angle ϕ for three levels of volume fraction of α_2 phase f_{α_2} at 5%, 15% and 25%, with $\lambda_D/\lambda_L = 20$. Hogging and sagging moments are represented by positive and negative ϕ respectively.

γ phase and with the enforcement of displacement compatibility in the $\alpha_2 - \gamma$ interface (and hence kinematic constraints), an increase in f_{α_2} contributes to the increase in induced bending moment, for a prescribed domain aspect ratio λ_D/λ_L. It is noteworthy that Lee et al. (1993) have reported that predominant pyramidal slips in α_2 phase (Umakoshi et al., 1993) tend to impose kinematic constraints to γ phase due to their high slip resistances when hard mode operates, refraining slip transmission from softer γ through to harder α_2 (Kad et al., 1995). The active slip systems here are similar to those in the previous subsection, in that they are transversal where two ordinary, four super and two pyramidal slip systems are operative during sagging while two ordinary, a super and two pyramidal slip systems are operative during hogging. The additional three super slips potentially results in the observed larger magnitude of $M/\tau_s^* V$ under sagging moments as compared with hogging moments.

Attention is now directed to overall bending moments at low bending angles to examine the onset of initial yield. Fig. 10 depicts the bending responses for $-0.015 \leq \phi \leq 0.015$ for the three levels of f_{α_2} and $\lambda_D/\lambda_L = 20$. Linear elastic relationships between $M/\tau_s^* V$ and ϕ are evident from the plot, wherein the elastic slopes are represented by the dashed lines and the initial yields are marked by solid circles. The overall bending moment at initial yield ($M_Y/\tau_s^* V$) displays an increasing trend with increasing f_{α_2} for both hogging and sagging moments, and that the bending angle at initial yield ϕ_Y exhibit a decreasing trend with increasing f_{α_2}, though the deviation appears relatively small between the respective ϕ_Y at each of the f_{α_2}. Computed values are tabulated in Table 7 for reference and comparison. An inspection of the bending normal stresses at initial yield reveals that $(\sigma_Y/\tau_s^*)_t$ and $(\sigma_Y/\tau_s^*)_c$ generally decrease as f_{α_2} increases, though the decrease is somewhat insignificant for $(\sigma_Y/\tau_s^*)_t$ under hogging and $(\sigma_Y/\tau_s^*)_c$ under sagging. In noting that during hogging, the topmost γ lamella and bottommost α_2 lamella are under states of tension and compression respectively and vice versa during sagging i.e. γ lamella and α_2 lamella in states of compression and tension respectively, the data suggests that the f_{α_2} has insignificant effects on the overall bending normal stresses in the topmost γ lamella. On the other hand, it is reported here that $(\sigma_Y/\tau_s^*)_t$ and $(\sigma_Y/\tau_s^*)_c$ in the α_2 lamella display a decreasing trend with increasing f_{α_2} under sagging and hogging moments respectively.

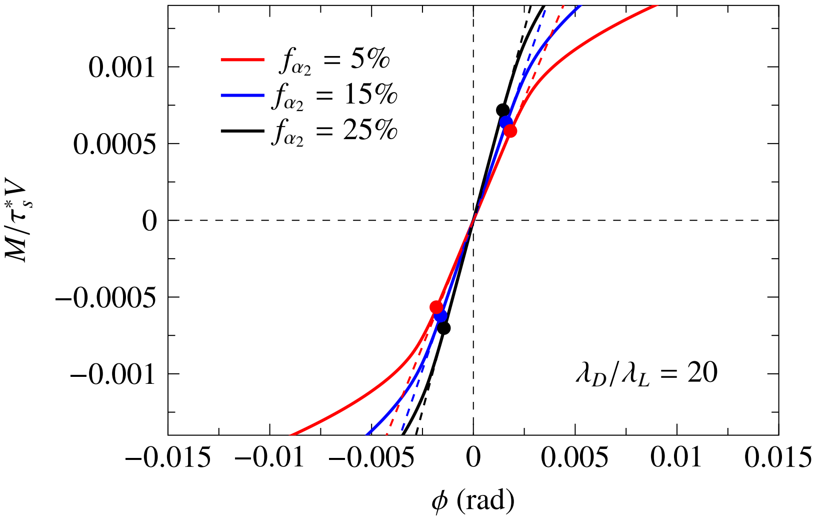

Fig. 10. Close–up view of Fig. 9 illustrating the linear relationship between $M/\tau_s^* V$ and ϕ at low bending angles, for the three levels of f_{α_2} and $\lambda_D/\lambda_L = 20$. Solid circles denote the initial yield in the overall response. Dashed lines represent the respective elastic slopes.

Table 7. List of values for bending moment, bending angle, tensile and compressive stresses at initial yield under both hogging and sagging moments for $f_{\alpha_2} = 5\%, 15\%, 25\%$ and $\lambda_D/\lambda_L = 20$.

Moment	f_{α_2}	ϕ_Y	$\left(\frac{M_Y}{\tau_s^* V}\right)$	$\left(\frac{\sigma_Y}{\tau_s^*}\right)_t$	$\left(\frac{\sigma_Y}{\tau_s^*}\right)_c$
Hogging	5%	1.82×10^{-3}	5.74×10^{-4}	0.0142	-0.0141
	15%	1.61×10^{-3}	6.29×10^{-4}	0.0141	-0.0137
	25%	1.45×10^{-3}	7.09×10^{-4}	0.0141	-0.0136
Sagging	5%	-1.82×10^{-3}	-5.74×10^{-4}	0.0141	-0.0142
	15%	-1.61×10^{-3}	-6.29×10^{-4}	0.0137	-0.0141
	25%	-1.45×10^{-3}	-7.20×10^{-4}	0.0136	-0.0141

3.4. Effect of constraints

The foregoing results have been obtained from a unit cell that has roller constraints imposed on X_1–X_2 planes at the two surfaces at $X_3 = \pm L_3$ along the X_3 direction, akin plane strain analyses. Note that it is strictly not plane strain analysis. It is, therefore, of interest to examine the effect of traction–free conditions on the overall bending responses of the PST TiAl. For tractability and brevity, we shall term the case of traction–free boundary conditions as ”relaxed condition”, and that with traction i.e. with imposed roller constraints as ”constrained condition”. The relaxed condition is accomplished by simply releasing the imposed roller conditions on the unit cell such that $u_3 \neq 0$. Specifically, we replace (13) by the traction–free condition $\sigma_{3j} n_j = 0$ where $n_j$is the orthonomal vector to the surfaces at $X_3 = \pm L_3$. Analyses are performed with parameters identical to those in Subsection 3.2 and Subsection 3.3. Fig. 11 and Fig. 12 depict the overall bending responses under relaxed conditions for varying λ_D/λ_L and f_{α_2} respectively. Bending responses under constrained conditions (see Subsection 3.2 and Subsection 3.3) are plotted together as dotted lines for comparison purposes.

It is immediately clear from the figures that relaxed conditions result in lower induced bending moments, and consequently bending resistance across all ϕ considered. This can be attributed to the active slip systems under relaxed and constrained conditions. In the relaxed conditions, the active slips under hogging are two ordinary slips, one superslip and two prismatic slips while under sagging, two ordinary slips, two superslips and two prismatic slips. In contrast under constrained conditions, two ordinary slips, one superslip and two pyramidal slips are active during hogging while two ordinary slips, four superslips and two pyramidal slips are active during sagging. As the slip resistance of prismatic slip is lower than that of pyramidal slip, the resulting induced bending moment under relaxed conditions at a prescribed bending angle is thus lower than under constrained conditions (see Table 4). Case in point if we consider the case of hogging wherein the only difference in the active slips under relaxed and constrained conditions are the activation of prismatic and pyramidal slips respectively.

It can be noted from Fig. 11 that the deviation of the bending moment responses at each level of λ_D/λ_L between the two constraints becomes greater as λ_D/λ_L decreases from 40 to 10. It is almost negligible at $\lambda_D/\lambda_L = 40$ as compared to that at $\lambda_D/\lambda_L = 10$. It is also observed that the profiles of the responses under relaxed condition are similar to those under constrained conditions. On the other hand from Fig. 12, the deviation in the bending moment responses between the two lateral constraints does not appear to vary with f_{α_2} i.e. deviations are near–constant (at any prescibed ϕ) at each level of f_{α_2} considered. The profiles of the responses under

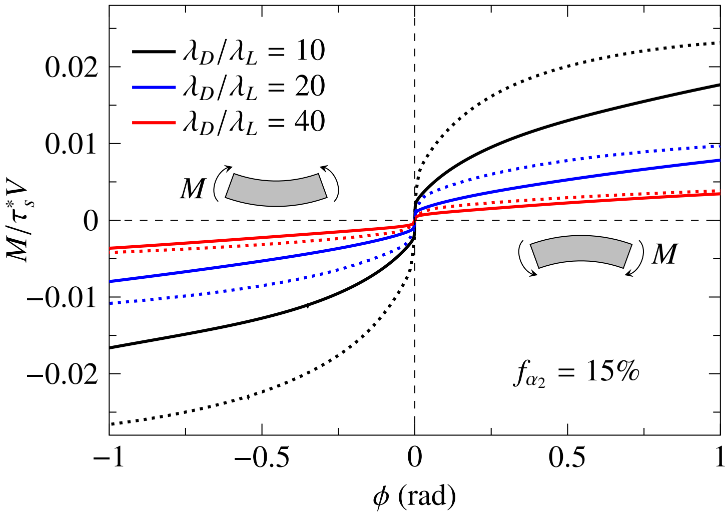

Fig. 11. Comparison of overall bending moment $M/\tau_s^* V$ with bending angle ϕ under constrained and relaxed conditions, for three levels of domain size aspect ratio $\lambda_D/\lambda_L = 10, 20$ and 40 with α_2 phase volume fraction, $f_{\alpha_2} = 15\%$. Dotted and solid lines represent cell's bending response under constrained and relaxed conditions respectively.

relaxed conditions are notably different from those under constrained conditions where in the former, the displayed responses appear almost linear for ϕ approximately greater than 0.25 rad. The stark differences in the bending responses under the two constraints, and under varying λ_D/λ_L and f_{α_2} are noteworthy due to the fact that the active slips are identical, considering the case of hogging in both Fig. 11 and Fig. 12. It can therefore be inferred that the bending behavior is affected predominantly by geometrical variations, in addition to the type of constraints imposed.

We now turn our attention to the various quantitites at initial yield under relaxed conditions. Table 8 lists the bending angle, bending moment, tensile and compressive stresses at initial yield under both hogging and sagging moments for $\lambda_D/\lambda_L = 10, 20, 40$ and $f_{\alpha_2} = 15\%$, while Table 9 lists the same quantities for $f_{\alpha_2} = 5\%, 15\%, 25\%$ and $\lambda_D/\lambda_L = 20$. Similar quantities under constrained conditions are also listed for ease of reference and comparison. An examination of the data presented in the tables reveal the lower bending moment $(M/\tau_s^* V)_Y$ and bending angle ϕ_Y at initial yield associated with relaxed conditions, in comparison with those with constrained conditions. The values of the maximum normal tensile and compressive stresses $(\sigma_Y/\tau_s^*)_t$ and $(\sigma_Y/\tau_s^*)_c$ respectively, are also observed to be comparatively lower under relaxed conditions.

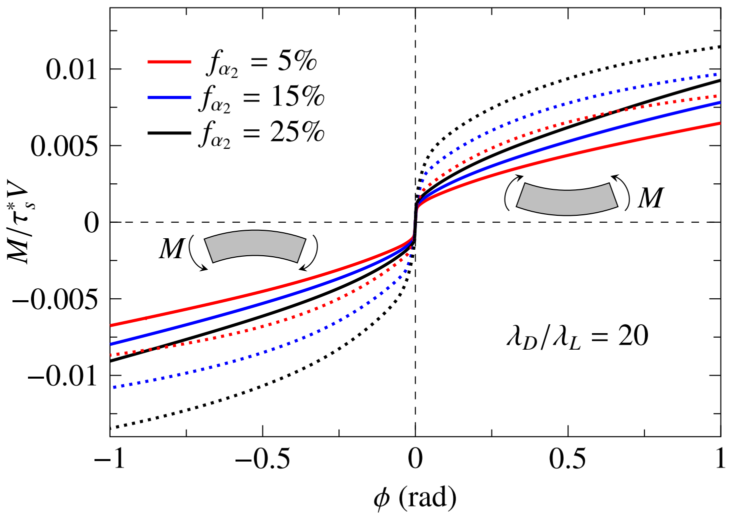

Fig. 12. Comparison of overall bending moment M/τ_s^*V with bending angle ϕ under constrained and relaxed conditions, for three levels of α_2 phase volume fraction $f_{\alpha_2} = 5\%, 15\%$ and 25%, with $\lambda_D/\lambda_L = 20$. Dotted and solid lines represent cell's bending response under constrained and relaxed conditions respectively.

Table 8. List of values for bending angle, bending moment, tensile and compressive stresses at initial yield under both hogging and sagging moments for $\lambda_D/\lambda_L = 10, 20, 40$ and $f_{\alpha_2} = 15\%$, under relaxed and constrained conditions.

		Relaxed conditions			
Moment	λ_D/λ_L	ϕ_Y	$\left(\frac{M}{\tau_s^*V}\right)_Y$	$\left(\frac{\sigma_Y}{\tau_s^*}\right)_t$	$\left(\frac{\sigma_Y}{\tau_s^*}\right)_c$
Hogging	10	8.13×10^{-4}	1.15×10^{-3}	0.0128	-0.0125
	20	1.58×10^{-3}	5.63×10^{-4}	0.0126	-0.0123
	40	3.02×10^{-3}	2.75×10^{-4}	0.0123	-0.0120
Sagging	10	-8.16×10^{-4}	-1.15×10^{-3}	0.0125	-0.0129
	20	-1.58×10^{-3}	-5.64×10^{-4}	0.0123	-0.0126
	40	-3.03×10^{-3}	-2.76×10^{-4}	0.0120	-0.0123
		Constrained conditions			
Moment	λ_D/λ_L	ϕ_Y	$\left(\frac{M}{\tau_s^*V}\right)_Y$	$\left(\frac{\sigma_Y}{\tau_s^*}\right)_t$	$\left(\frac{\sigma_Y}{\tau_s^*}\right)_c$
Hogging	10	8.23×10^{-4}	1.28×10^{-3}	0.0144	-0.0140
	20	1.61×10^{-3}	6.25×10^{-4}	0.0140	-0.0136
	40	3.21×10^{-3}	3.04×10^{-4}	0.0136	-0.0132
Sagging	10	-8.29×10^{-4}	-1.29×10^{-3}	0.0141	-0.0145
	20	-1.61×10^{-3}	-6.28×10^{-4}	0.0137	-0.0141
	40	-3.20×10^{-3}	-3.13×10^{-4}	0.0136	-0.0140

4. Concluding remarks

Micromechanical analyses *via* CPFEM on the bending behavior of a single polysynthetically twinned (PST) titanium aluminide (TiAl) colony comprising one α_2-Ti_3Al layer and six γ-TiAl layers have been performed. Each γ layer is made up of hexagonal–shaped domains, such that

Table 9. List of values for bending moment, bending angle, tensile and compressive stresses at initial yield under both hogging and sagging moments for $f_{\alpha_2} = 5\%, 15\%, 25\%$ and $\lambda_D/\lambda_L = 20$, under relaxed and constrained conditions.

		Relaxed conditions			
Moment	f_{α_2}	ϕ_Y	$\left(\frac{M}{\tau_s^* V}\right)_Y$	$\left(\frac{\sigma_Y}{\tau_s^*}\right)_t$	$\left(\frac{\sigma_Y}{\tau_s^*}\right)_c$
Hogging	5%	1.70×10^{-3}	4.90×10^{-4}	0.0122	-0.0120
	15%	1.58×10^{-3}	5.44×10^{-4}	0.0122	-0.0119
	25%	1.31×10^{-3}	6.12×10^{-4}	0.0122	-0.0117
Sagging	5%	-1.70×10^{-3}	-4.91×10^{-4}	0.0121	-0.0122
	15%	-1.58×10^{-3}	-5.44×10^{-4}	0.0119	-0.0122
	25%	-1.31×10^{-3}	-5.98×10^{-4}	0.0114	-0.0119
		Constrained conditions			
Moment	f_{α_2}	ϕ_Y	$\left(\frac{M}{\tau_s^* V}\right)_Y$	$\left(\frac{\sigma_Y}{\tau_s^*}\right)_t$	$\left(\frac{\sigma_Y}{\tau_s^*}\right)_c$
Hogging	5%	1.82×10^{-3}	5.74×10^{-4}	0.0142	-0.0141
	15%	1.61×10^{-3}	6.29×10^{-4}	0.0141	-0.0137
	25%	1.45×10^{-3}	7.09×10^{-4}	0.0141	-0.0136
Sagging	5%	-1.82×10^{-3}	-5.74×10^{-4}	0.0141	-0.0142
	15%	-1.61×10^{-3}	-6.29×10^{-4}	0.0137	-0.0141
	25%	-1.45×10^{-3}	-7.20×10^{-4}	0.0136	-0.0141

the colony is characterized by two length scales namely the lamella thickness λ_L and domain size λ_D. The analyses examine on the effects of domain size aspect ratio λ_D/λ_L, volume fraction of α_2 phase f_{α_2} and lateral constraints on the bending behavior of PST crystal of TiAl, wherein the former refers the imposition of generalized plane strain and plane stress conditions on the longitudinal faces of the unit cell.

The bending analyses show that a lower λ_D/λ_L and higher f_{α_2} increase the induced bending moment or bending resistance for the range of prescribed bending angles ϕ, regardless of the constraints imposed. Varying λ_D/λ_L and f_{α_2} essentially alter the second moment of cross–sectional area I, where it is known from classical beam theory that I is proportional to bending moment. Here, a lower λ_D/λ_L (implying a higher λ_L for a fixed λ_D) or higher f_{α_2} (a higher λ_{α_2}) results in a larger value of I, all other dimensions remaining unchanged. In addition to the contribution of I, a thicker lamella results in an increase in the maximum number of dislocations per slip plane, leading to observed higher induced bending moment and material hardening responses. At this juncture, the numerical results reveal that the type and number of slip systems activated during bending appear to be independent of λ_D/λ_L and f_{α_2}, but dependent on the bending mode i.e. hogging or sagging moments as well as the constraints imposed. Under constrained conditions, the active slip systems are

- 2 ordinary slips, 1 superslip and 2 pyramidal slips (hogging)
- 2 ordinary slips, 4 superslips and 2 pyramidal slips (sagging)

whereas under relaxed conditions,

- 2 ordinary slips, 1 superslip and 2 prismatic slips (hogging)

- 2 ordinary slips, 2 superslips and 2 prismatic slips (sagging)

The additional superslip systems during sagging bring about the comparatively higher bending moments in comparison to those under hogging, resulting in the asymmetrical bending moment responses. Imposing traction–free boundary conditions (relaxed condition) activate prismatic slips in the α_2 phase, in contrast to pyramidal slips that are activated when plane strain boundary conditions are imposed (constrained condition). As the slip resistance of prismatic slip is lower than pyramidal slip, the induced bending moments in all the cases of λ_D/λ_L and f_{α_2} considered under relaxed conditions are thus lower than the bending moments under constrained condition (see Fig. 11 and Fig. 12).

The bending moment–bending angle diagrams exhibit response profiles similar to the familiar uniaxial stress–strain and/or force–displacement curves, where linear and non–linear regimes can be identified from which the initial yield in the elastic limit corresponding to the onset of initial slip activities can be established. The corresponding overall bending moment at initial yield (M_Y/τ_s^*V) is used to obtain the initial overall maximum tensile and compressive yield stresses $(\sigma_Y/\tau_s^*)_t$ and $(\sigma_Y/\tau_s^*)_c$ respectively. The analyses have shown that (M_Y/τ_s^*V) increases as λ_D/λ_L decreases and as f_{α_2} increases. At the same time, the bending angle ϕ_Y at which the initial yield occurs displays a decreasing trend with the same variations of λ_D/λ_L and f_{α_2}. As alluded to previously, it can be inferred that the trends of (M_Y/τ_s^*V) and ϕ_Y are due solely to geometrical variations and consequently the second moment of area, given that the slips systems being activated are not influenced by the domain size aspect ratio and volume fraction of α_2 phase.

The effects of λ_D/λ_L and f_{α_2} on $(\sigma_Y/\tau_s^*)_t$ and $(\sigma_Y/\tau_s^*)_c$ are shown to be significant, regardless of the imposed constraints. While $(\sigma_Y/\tau_s^*)_t$ and $(\sigma_Y/\tau_s^*)_c$ exhibit decreasing trends as λ_D/λ_L increases for both of the two bending modes of hogging and sagging, their trends are different when f_{α_2} is varied. $(\sigma_Y/\tau_s^*)_t$ and $(\sigma_Y/\tau_s^*)_c$ display increasing trends only under sagging and hogging moments respectively as f_{α_2} decreases, while $(\sigma_Y/\tau_s^*)_t$ under hogging and $(\sigma_Y/\tau_s^*)_c$ under sagging remains relatively constant. In noting that during sagging, maximum normal tensile stresses develop in the α_2 lamella and maximum normal compressive stresses in the γ lamalla (and vice–versa during hogging, following the stacking configuration in Fig. 2), the results signify that f_{α_2} has insignificant effect on the overall maximum tensile and compressive yield stresses in the topmost γ lamalla.

In summary, the results presented here indicate that bending moment of PST TiAl can be tuned by geometrical variations i.e. varying the domain size aspect ratio and/or volume fraction of α_2 which essentially tune the second moment of area, or by constraints where pyramidal or prismatic slip systems can be selectively activated. Indeed, Umakoshi et al. (1993) have reported that the deformation mode of α_2 phase is significant and that the pyramidal slip in the said phase is effective in strengthening due to its role as a barrier for increasing dislocation pile–ups in the γ phase. This paper seeks to provide insights to the microstructure–property relationship of PST TiAl subjected to bending, which the authors consider to be in an infancy stage of research. This is in comparison with large body of work and research on PST TiAL subjected to uniaxial tension/compression. As such, there are opportunities and much to be explored in the quest to seek deeper understanding of the microstructure–property relationship of PST TiAl under bending. Some areas of research may include the various configurations or stacking sequences of γ and α_2 lamellae e.g. $(3\alpha_2 + 6\gamma)$ or any other permutations and combinations of the phases, or the effects of misorientations and non–coherent α_2/γ interfaces.

Acknowledgments — We gratefully acknowledge the support of this work by Structural Metal Alloys Programme and the Agency for Science and Technology Research, A*STAR (Grant No:

A18B1b0061). The authors thank Prof. Huajian Gao for the fruitful and insightful discussions.

Appendix A. Elastic stiffness matrix for TiAl single crystals

Voigt notation in ABAQUS is used to express the linear elastic stress-strain relations for TiAl single crystals:

- For tetragonal crystal γ-TiAl ($\mathbf{e}_1 \| \boldsymbol{a}$)

$$\begin{pmatrix} \sigma_{11} \\ \sigma_{22} \\ \sigma_{33} \\ \sigma_{12} \\ \sigma_{13} \\ \sigma_{23} \end{pmatrix} = \begin{pmatrix} C_{11} & C_{12} & C_{13} & 0 & 0 & 0 \\ C_{12} & C_{11} & C_{13} & 0 & 0 & 0 \\ C_{13} & C_{13} & C_{33} & 0 & 0 & 0 \\ 0 & 0 & 0 & C_{44} & 0 & 0 \\ 0 & 0 & 0 & 0 & C_{44} & 0 \\ 0 & 0 & 0 & 0 & 0 & C_{66} \end{pmatrix} \begin{pmatrix} \varepsilon_{11} \\ \varepsilon_{22} \\ \varepsilon_{33} \\ 2\varepsilon_{12} \\ 2\varepsilon_{13} \\ 2\varepsilon_{23} \end{pmatrix} \tag{A.1}$$

  The stiffness matrix has 6 independent elastic constants; refer to their values in Table 2.

- For hexagonal crystal α_2-Ti_3Al ($\mathbf{e}_3 \| \boldsymbol{c}$)

$$\begin{pmatrix} \sigma_{11} \\ \sigma_{22} \\ \sigma_{33} \\ \sigma_{12} \\ \sigma_{13} \\ \sigma_{23} \end{pmatrix} = \begin{pmatrix} C_{11} & C_{12} & C_{13} & 0 & 0 & 0 \\ C_{12} & C_{11} & C_{13} & 0 & 0 & 0 \\ C_{13} & C_{13} & C_{33} & 0 & 0 & 0 \\ 0 & 0 & 0 & C_{44} & 0 & 0 \\ 0 & 0 & 0 & 0 & C_{44} & 0 \\ 0 & 0 & 0 & 0 & 0 & \frac{C_{11}-C_{12}}{2} \end{pmatrix} \begin{pmatrix} \varepsilon_{11} \\ \varepsilon_{22} \\ \varepsilon_{33} \\ 2\varepsilon_{12} \\ 2\varepsilon_{13} \\ 2\varepsilon_{23} \end{pmatrix} \tag{A.2}$$

  The stiffness matrix has 5 independent elastic constants; refer to their values in Table 3.

Appendix B. Bending moment calculation

In the undeformed reference configuration, balance of linear and angular momentum has the local forms

$$P_{iJ,J} = 0, \quad (\epsilon_{imn} x_m P_{nJ})_{,J} = 0 \tag{B.1}$$

respectively, in the absence of body forces, where P_{iJ} is the first Piola-Kirchhoff stress in Cartesian coordinate system, x_m the position vector in the current deformed configuration, and ϵ_{imn} the alternating tensor. Using the divergence theorem, the above balance has the integral forms

$$\oint \boldsymbol{P} \cdot d\boldsymbol{S} = 0, \quad \oint \boldsymbol{x} \times \boldsymbol{P} \cdot d\boldsymbol{S} = 0 \tag{B.2}$$

over a closed surface with oriented differential element $d\boldsymbol{S}$ in the undeformed reference configuration.

(B.2)$_2$ helps in identifying the moment (around a point) for bending or torsion. To see this, we begin with the virtual work equation

$$\int_V \boldsymbol{P} : \delta \boldsymbol{F} dV = \int_{\partial V} \delta \boldsymbol{x} \cdot \boldsymbol{P} \cdot d\boldsymbol{S}. \tag{B.3}$$

on certain portion of outer surface ∂V. Imposing orthogonal rotations on outer cross-sections of the body

$$\boldsymbol{x} = \boldsymbol{R} \cdot \boldsymbol{X} \quad \text{on } S_m \subset \partial V \tag{B.4}$$

gives

$$\begin{aligned} \delta \boldsymbol{x} &= \delta \boldsymbol{R} \cdot \boldsymbol{X} = \underbrace{\delta \boldsymbol{R} \cdot \boldsymbol{R}^{-1}}_{\delta \boldsymbol{\Omega}} \cdot \boldsymbol{x} \quad (\delta \boldsymbol{\Omega} = -\boldsymbol{\epsilon} \cdot \delta \boldsymbol{\theta}) \\ &= \delta \boldsymbol{\theta} \times \boldsymbol{x} \end{aligned} \tag{B.5}$$

where $\boldsymbol{R}$ is the orthogonal tensor, and $\delta \boldsymbol{\Omega}$ is skew-symmetric and can be expressed in terms of the axial vector $\delta \boldsymbol{\theta}$ (infinitesimal rotation).

Assume that on $\partial V \cap S_m$ there is either no surface traction ($\boldsymbol{P} \cdot d\boldsymbol{S} = 0$) or no surface displacement ($\delta \boldsymbol{x} = 0$). Then inserting (B.5) into (B.3) leads to

$$\int_V \boldsymbol{P} : \delta \boldsymbol{F} dV = \boldsymbol{M} \cdot \delta \boldsymbol{\theta} \tag{B.6}$$

where

$$\boldsymbol{M} = \int_{S_m} \boldsymbol{x} \times \boldsymbol{P} \cdot d\boldsymbol{S}. \tag{B.7}$$

When equal and opposite rotations are imposed on the cross-sections of the cuboid RVE at $X_1 = \pm L_1$, we have $\delta \boldsymbol{\theta} = \mp \delta \phi \mathbf{e}_3$ ($\mathbf{e}_3$ is the basis vector), from which we can easily obtain (14) and (15), where the bending moment is calculated around the moving point $(X_1, X_2 + Y_0, X_3)$.

Using Nanson's formula

$$d\boldsymbol{s} = J \boldsymbol{F}^{-T} \cdot d\boldsymbol{S} \tag{B.8}$$

and the relationship

$$\boldsymbol{P} = J \boldsymbol{\sigma} \cdot \boldsymbol{F}^{-T} \tag{B.9}$$

between $\boldsymbol{P}$ and the Cauchy stress $\boldsymbol{\sigma}$ (which is related to the Kirchhoff stress by $\boldsymbol{\tau} = J\boldsymbol{\sigma}$ with $J = \det \boldsymbol{F}$), we have

$$\boldsymbol{P} \cdot d\boldsymbol{S} = \boldsymbol{\sigma} \cdot d\boldsymbol{s} \tag{B.10}$$

such that the moment $\boldsymbol{M}$ (B.7) can also be calculated in the current deformed configuration

$$\boldsymbol{M} = \int_{S_m} \boldsymbol{x} \times \boldsymbol{P} \cdot d\boldsymbol{S} = \int_{s_m} \boldsymbol{x} \times \boldsymbol{\sigma} \cdot d\boldsymbol{s}. \tag{B.11}$$

References

ABAQUS Version 6.14, 2014. User's Manual Version 6.14. Dassault Systèmes Simulia Corp, Providence, RI, USA.

Antolovich, S.D., Armstrong, R.W., 2014. Plastic strain localization in metals: origins and consequences. Prog. Mater. Sci. 59, 1–160.

Appel, F., Paul, J.D.H., Oehring, M., 2011. Gamma titanium aluminide alloys: science and technology. John Wiley & Sons.

Appel, F., Wagner, R., 1998. Microstructure and deformation of two-phase γ-titanium aluminides. Mater. Sci. Engng. Rep. 22, 187–268.

Arata, J.J.M., Kumar, K.S., Curtin, W.A., Needleman, A., 2001. Crack growth in lamellar titanium aluminide. Int. J. Fract. 111, 163–189.

Asaro, R.J., Rice, J.R., 1977. Strain localization in ductile single crystals. J. Mech. Phys. Solids 25, 309–338.

Blackburn, M.J., 1970. The science, technology and application of titanium.

Cao, R., Li, L., Chen, J.H., Zhang, J., He, H., 2010. Study on compression deformation, damage and fracture behaviour of TiAl alloys: Part I. deformation and damage behaviour. Mater. Sci. Eng. A 527, 2455–2467.

Chen, G., Peng, Y., Zheng, G., Qi, Z., Wang, M., Yu, H., Dong, C., Liu, C.T., 2016. Polysynthetic twinned TiAl single crystals for high-temperature applications. Nat. Mater. 15, 876–881.

Chen, L., Edwards, T.E.J., Di Gioacchino, F., Clegg, W.J., Dunne, F.P., Pham, M.S., 2019. Crystal plasticity analysis of deformation anisotropy of lamellar TiAl alloy: 3D microstructure-based modelling and in-situ micro-compression. Int. J. Plast. 119, 344–360.

Cheng, L., Guo, T.F., 2007. Void interaction and coalescence in polymeric materials. Int. J. Solids Struct. 44, 1787–1808.

Chlupova, A., Heczko, M., Obrtlík, K., Dlouhỳ, A., Kruml, T., 2020. Effect of heat-treatment on the microstructure and fatigue properties of lamellar γ-TiAl alloyed with Nb, Mo and/or C. Mater. Sci. Eng. A 786, 139427.

Cleveringa, H.H.M., Van der Giessen, E., Needleman, A., 1999. A discrete dislocation analysis of bending. Int. J. Plast. 15, 837–868.

Cornec, A., Kabir, M.R., Huber, N., 2015. Numerical prediction of the stress–strain response of a lamellar γTiAl polycrystal using a two-scale modelling approach. Mater. Sci. Eng. A 620, 273–285.

Dimiduk, D.M., Hazzledine, P.M., Parthasarathy, T.A., Mendiratta, M.G., Seshagiri, S., 1998. The role of grain size and selected microstructural parameters in strengthening fully lamellar TiAl alloys. Metall. Mater. Trans. A 29, 37–47.

Ding, R.G., Chiu, Y.L., Chu, M.Q., Paddea, S., Su, G.Q., 2020. A study of fracture behaviour of gamma lamella using the notched TiAl micro-cantilever. Philos. Mag. 100, 982–997.

Du, Z.L., Zhang, G., Guo, T.F., Tang, S., Guo, X., 2020. Tension-compression asymmetry at finite strains: A theoretical model and exact solutions. J. Mech. Phys. Solids 143, 104084.

Fleck, N.A., Muller, G.M., Ashby, M.F., Hutchinson, J.W., 1994. Strain gradient plasticity: theory and experiment. Acta Metall. Mater. 42, 475–487.

Fu, C.L., Yoo, M.H., 1990. Elastic constants, fault energies, and dislocation reactions in TiAl: A first-principles total-energy investigation. Philos. Mag. Lett. 62, 159–165.

Fujiwara, T., Nakamura, A., Hosomi, M., Nishitani, S.R., Shirai, Y., Yamaguchi, M., 1990. Deformation of polysynthetically twinned crystals of TiAl with a nearly stoichiometric composition. Philos. Mag. A 61, 591–606.

Geers, M.G.D., Kouznetsova, V., Brekelmans, W.A.M., 2010. Multi-scale computational homogenization: Trends and challenges. J. Comput. Appl. Math. 234, 2175–2182.

Grujicic, M., Batchu, S., 2001. A crystal plasticity materials constitutive model for polysynthetically-twinned γ-TiAl + α_2-Ti_3Al single crystals. J. Mater. Sci. 36, 2851–2863.

Grujicic, M., Cao, G., Batchu, S., 2003a. Crystal plasticity-based finite element analysis of deformation and fracture of polycrystalline lamellar γ-TiAl+ α_2-Ti_3Al alloys. J. Mater. Sci. 38, 307–322.

Grujicic, M., Cao, G., Joseph, P.F., 2003b. Multiscale modeling of deformation and fracture of polycrystalline lamellar γ-TiAl + α_2-Ti_3Al alloys. Int. J. Multiscale Comput. Eng. 1.

Gu, X.W., Greer, J.R., 2015. Ultra-strong architected Cu meso-lattices. Extreme Mech. Lett. 2, 7–14.

Guo, T.F., Wong, W.H., 2018. Void-sheet analysis on macroscopic strain localization and void coalescence. J. Mech. Phys. Solids 118, 172–203.

Harren, S.V., Asaro, R.J., 1989. Nonuniform deformations in polycrystals and aspects of the validity of the Taylor model. J. Mech. Phys. Solids 37, 191–232.

Hazzledine, P.M., Kad, B.K., 1995. Yield and fracture of lamellar γ/α_2 TiAl alloys. Mater. Sci. Eng. A 192, 340–346.

Hill, R., Rice, J.R., 1972. Constitutive analysis of elastic-plastic crystals at arbitrary strain. J. Mech. Phys. Solids 20, 401–413.

Huang, L., 2005. Microstructural evolution of TiAl-intermetallic alloys containing W and B .

Hutchinson, J.W., 1976. Bounds and self-consistent estimates for creep of polycrystalline materials. Proc. R. Soc. A 348, 101–127.

Inui, H., Oh, M., Nakamura, A., Yamaguchi, M., 1992a. Room-temperature tensile deformation of polysynthetically twinned (PST) crystals of TiAl. Acta Metall. Mater. 40, 3095–3104.

Inui, H., Oh, M.H., Nakamura, A., Yamaguchi, M., 1992b. Ordered domains in TiAl coexisting with Ti_3Al in the lamellar structure of Ti-rich TiAl compounds. Philos. Mag. A 66, 539–555.

Kabir, M.R., Chernova, L., Bartsch, M., 2010. Numerical investigation of room-temperature deformation behaviour of a duplex type γTiAl alloy using a multi-scale modeling approach. Acta Mater. 58, 5834–5847.

Kad, B.K., Dao, M., Asaro, R.J., 1995. Numerical simulations of plastic deformation and fracture effects in two phase γ-TiAl+ α_2-Ti_3Al lamellar microstructures. Philos. Mag. A 71, 567–604.

Kanani, M., Hartmaier, A., Janisch, R., 2016. Stacking fault based analysis of shear mechanisms at interfaces in lamellar TiAl alloys. Acta Mater. 106, 208–218.

Kim, Y.W., 1992. Microstructural evolution and mechanical properties of a forged gamma titanium aluminide alloy. Acta Metall. Mater. 40, 1121–1134.

Kim, Y.W., 1998. Strength and ductility in TiAl alloys. Intermetallics 6, 623–628.

Kothari, M., 1997. Polycrystalline elasto-viscoplasticity: application to BCC metals. Ph.D. thesis. Massachusetts Institute of Technology.

Kouznetsova, V., Geers, M.G.D., Brekelmans, W.A.M., 2002. Multi-scale constitutive modelling of heterogeneous materials with a gradient-enhanced computational homogenization scheme. Int. J. Numer. Methods Eng. 54, 1235–1260.

Lebensohn, R., Uhlenhut, H., Hartig, C., Mecking, H., 1998. Plastic flow of γ-TiAl-based polysynthetically twinned crystals: micromechanical modeling and experimental validation. Acta Mater. 46, 4701–4709.

Lee, B.J., Ahzi, S., Kad, B.K., Asaro, R.J., 1993. On the deformation mechanisms in lamellar Ti-Al alloys. Scripta Metall. 29.

Li, T.R., Liu, G.H., Xu, M., Fu, T.L., Tian, Y., Misra, R.J.D.K., Wang, Z.D., 2018. Hot deformation behaviour and microstructural characteristics of ti–46al–8nb alloy. Acta Metall. Sin. 31, 933–944.

Li, W., Yin, Y., Xu, Q., Zhou, J., Nan, H., Ji, X.Y., Shen, X., Feng, X., Yu, W., Tu, Z.X., et al., 2019. Tensile behaviour of γ/α_2 interface system in lamellar TiAl alloy via molecular dynamics. Comput. Mater. Sci. 159, 397–402.

Liu, X.W., Su, Y.Q., Luo, L.S., Liu, J.p., Guo, J.J., Fu, H.Z., 2010. Effect of hydrogen on hot deformation behaviours of TiAl alloys. Int. J. Hydrog. Energy 35, 13322–13328.

Liu, Z.G., Wong, W.H., Guo, T.F., 2016. Void behaviours from low to high triaxialities: Transition from void collapse to void coalescence. Int. J. Plast. 84, 183–202.

Ma, R., Pilchak, A.L., Semiatin, S.L., Truster, T.J., 2018. Modeling the evolution of microtextured regions during α/β processing using the crystal plasticity finite element method. Int. J. Plast. 107, 189–206.

Maziasz, P.J., Liu, C.T., 1998. Development of ultrafine lamellar structures in two-phase γ-TiAl alloys. Metall. Mater. Trans. A 29, 105–117.

Mine, Y., Fujisaki, H., Matsuda, M., Takeyama, M., Takashima, K., 2011. Microtension behaviour of TiAl polysynthetically twinned crystals with 0°-and 90°-oriented lamellae. Scr. Mater. 65, 707–710.

Nakano, T., Yokoyama, A., Umakoshi, Y., 1992. Effect of Nb addition on the plastic behaviour of TiAl crystals containing oriented lamellae. Scripta Metall. Mater. 27, 1253–1258.

Palomares-García, A.J., Pérez-Prado, M.T., Molina-Aldareguia, J.M., 2017. Effect of lamellar orientation on the strength and operating deformation mechanisms of fully lamellar TiAl alloys determined by micropillar compression. Acta Mater. 123, 102–114.

Qiu, H., Ueji, R., Kimura, Y., Inoue, T., 2020. Heterogeneous distribution of microstrain evolved during tensile deformation of polycrystalline plain low carbon steel. Metals 10, 774.

Schlögl, S.M., Fischer, F.D., 1997. The role of slip and twinning in the deformation behaviour of polysynthetically twinned crystals of TiAl: a micromechanical model. Philos. Mag. A 75, 621–636.

Schnabel, J.E., 2018. Crystal plasticity modeling of fully lamellar titanium aluminide alloys. Ph.D. thesis. Technische Universität Hamburg.

Schütze, M., 2016. Single-crystal performance boost. Nat. Mater. 15, 823–824.

Schwaighofer, E., Clemens, H., Mayer, S., Lindemann, J., Klose, J., Smarsly, W., Güther, V., 2014. Microstructural design and mechanical properties of a cast and heat-treated intermetallic multi-phase γ-TiAl based alloy. Intermetallics 44, 128–140.

Song, L., Appel, F., Wang, L., Oehring, M., Hu, X., Stark, A., He, J., Lorenz, U., Zhang, T., Lin, J., et al., 2020. New insights into high-temperature deformation and phase transformation mechanisms of lamellar structures in high Nb-containing TiAl alloys. Acta Mater. 186, 575–586.

Su, Y., Zambaldi, C., Mercier, D., Eisenlohr, P., Bieler, T.R., Crimp, M.A., 2016. Quantifying deformation processes near grain boundaries in α titanium using nanoindentation and crystal plasticity modeling. Int. J. Plast. 86, 170–186.

Teng, C.Y., Zhou, N., Wang, Y., Xu, D.S., Du, A., Wen, Y.H., Yang, R., 2012. Phase-field simulation of twin boundary fractions in fully lamellar TiAl alloys. Acta Mater. 60, 6372–6381.

Umakoshi, Y., Nakano, T., Takenaka, T., Sumimoto, K., Yamane, T., 1993. Orientation and temperature dependence of yield stress and slip geometry of Ti_3Al and Ti_3Al-V single crystals. Acta Metall. Mater. 41, 1149–1154.

Umeda, H., Kishida, K., Inui, H., Yamaguchi, M., 1997. Effects of Al-concentration and lamellar spacing on the room-temperature strength and ductility of PST crystals of TiAl. Mater. Sci. Eng. A 239, 336–343.

Wang, F., Wang, G., Ji, L., Zeng, D., 2019. Effects of different temperatures on the lamellar structure evolution in γ–tial alloys: A phase-field study. Comp. Mater. Sci. 164, 22–30.

Werwer, M., Cornec, A., 2000. Numerical simulation of plastic deformation and fracture in polysynthetically twinned (PST) crystals of TiAl. Comput. Mater. Sci. 19, 97–107.

Werwer, M., Cornec, A., 2006. The role of superdislocations for modeling plastic deformation of lamellar TiAl. Int. J. Plast. 22, 1683–1698.

Werwer, M., Kabir, R., Cornec, A., Schwalbe, K.H., 2007. Fracture in lamellar TiAl simulated with the cohesive model. Eng. Fract. Mech. 74, 2615–2638.

Wong, W.H., Guo, T.F., 2015. On the energetics of tensile and shear void coalescences. J. Mech. Phys. Solids 82, 259–286.

Yamaguchi, M., Inui, H., Ito, K., 2000. High-temperature structural intermetallics. Acta Mater. 48, 307–322.

Yoo, M.H., Zou, J., Fu, C.L., 1995. Mechanistic modeling of deformation and fracture behaviour in TiAl and Ti_3Al. Mater. Sci. Eng. A 192, 14–23.

You, Z.S., Li, X.Y., Gui, L.J., Lu, Q.H., Zhu, T., Gao, H.J., Lu, L., 2013. Plastic anisotropy and associated deformation mechanisms in nanotwinned metals. Acta Mater. 61, 217–227.

Yu, Q., Wen, D., Wang, S., Kong, B., Wu, S., Xiao, T., 2020. Effect of 0.8 at.% h on the mechanical properties and microstructure evolution of a Ti-45Al-9Nb alloy under uniaxial tension at high temperature. Coatings 10, 52.

Zambaldi, C., Roters, F., Raabe, D., 2011. Analysis of the plastic anisotropy and pre-yielding of (γ/α_2)-phase titanium aluminide microstructures by crystal plasticity simulation. Intermetallics 19, 820–827.

Zeng, Y.P., Li, X.Y., 2021. Atomistic simulations of high-temperature creep in nanotwinned TiAl alloys. Extreme Mech. Lett. 44, 101253.

Zhang, L.C., Chen, G.L., Wang, J.G., Ye, H.Q., 1998. TEM study on lamellar microstructure and α_2/γ interfacial structure in a hot-deformed two-phase γ-TiAl-based alloy. Mater. Sci. Eng. A 247, 1–7.

Zhang, T.L., Wang, D., Zhu, J.M., Xiao, H., Liu, C., Wang, Y.Z., 2020. Non-conventional transformation pathways and ultrafine lamellar structures in γ-TiAl alloys. Acta Mater. 189, 25–34.

Zhu, H., Seo, D., Maruyama, K., Au, P., 2006. Effect of lamellar spacing on microstructural instability and creep behaviour of a lamellar TiAl alloy. Scr. Mater. 54, 1979–1984.

Zong, Y.Y., Wen, D.S., Guo, B., Shan, D.B., 2015. Investigations of hydrogen-promoted α_2-lamella decomposition of a γ-TiAl based alloy. Mater. Lett. 152, 196–199.